A Monte Carlo Calculation of Virtual Source Size and

Energy Spread for a Liquid Metal Ion Source

Patrick J. Hoepfner

B.S. in Physics, Seattle University, 1981

A thesis submitted to the faculty

of the Oregon Graduate Center

in partial fulfillment of the

requirements for the degree

Master of Science

in

Applied Physics

January, 1985

The thesis "A Monte Carlo Calculation of Virtual Source Size and Energy Spread for a Liquid Metal Ion Source" by Patrick Hoepfner has been examined and approved by the following examination committee.

Lynwood W. Swanson
Professor

Richard A. Elliott
Professor

John S. Blakemore
Professor

M.A.K. Khalil
Professor

ACKNOWLEDGEMENTS

ABSTRACT

A Monte Carlo Calculation of Virtual Source Size and
Energy Spread for a Liquid Metal Ion Source

Patrick J. Hoepfner, M.S.
Oregon Graduate Center

Supervising Professor: Lynwood W. Swanson

It has been recently observed that the virtual source size and energy spread
increases with current for liquid metal ion sources. It is important to know how the
energy spread and virtual source size depend on all of the experimental parameters.

The Monte Carlo method was employed to simulate the natural emission
process for a liquid metal ion source. Each of the ions was traced from a spherical
emitter to a final reference plane while under the influences of the spherical
accelerating field and the mutual interactions of the other ions. At the final refer-
ence plane the velocities and positions were determined. From these values the final
energy spread and virtual source size were obtained. To find the functional depen-
dence of all of the experimental parameters, the program was rerun varying one
parameter at a time over a specific range of values. The experimental parameters
investigated were: current (I), mass (M), charge (q), emitter radius (a), field at the
emitter surface (F), distance traveled by the ions (Z), emission angle (α), initial
kinetic energy, and initial energy spread of the ions.

In the final analysis, the functional dependence of the energy spread ΔE and
the virtual source diameter d, on the various parameters was found to be dimen-
sionally consistent. They are:

$$\Delta E \propto \frac{I}{\alpha} \left[\frac{Mq}{Fa} \right]^{1/2}$$

and

$$d \propto \frac{1}{\alpha F} \left[\frac{IM^{1/2}Z^{1/2}}{a} \right]^{1/2} .$$

The virtual source size and final energy spread were found to have no dependence on the initial kinetic energy, and the virtual source size was also found to be independent of the initial energy spread. The final energy spread, however, was found to be proportional to the initial energy spread.

Definitions:

a $\equiv$ Emitter Radius

d $\equiv$ Virtual Source Size

E_i $\equiv$ Initial Kinetic Energy

ΔE_i $\equiv$ Initial Kinetic Energy Spread

F $\equiv$ Surface Electric Field

I $\equiv$ Current

J $\equiv$ Current Density

M $\equiv$ Atomic Mass

N $\equiv$ Number of Steps

n $\equiv$ Number of Particles

q $\equiv$ Ionic Charge

T $\equiv$ Emission Time

t $\equiv$ Transit Time

Δt $\equiv$ Step Time

V_r $\equiv$ Applied Potential

V_t $\equiv$ Transverse Potential

Z $\equiv$ Flight Path Length

α $\equiv$ Beam Half Angle

$\bar{\tau}$ $\equiv$ Average Time Between Particles

Relationships:

$$\bar{\tau} = \frac{e}{I}$$

$$I = \frac{nqe}{T}$$

$$\Delta t = \frac{t}{N}$$

$$J = \frac{I}{2\pi a^2 (1-\cos\alpha)}$$

$$t = \left[\frac{m}{2qeFa}\right]^{1/2} \left\{ZA^{1/2} - \frac{a}{2}\ln\left[1 - \frac{A^{1/2}}{1} + A^{1/2}\right]\right\}$$

For the case of no mutual interactions, where:

$$A \equiv 1 - \frac{a}{Z}$$

1. Introduction

There are many reasons for studying the virtual source size and energy spread of a beam of charged particles emitted from a field emitter. Apart from the fundamental reasons, these parameters place a lower limit on the focused spot size that can be expected from any electron/ion optical system. The energy spread determines the magnitude of the chromatic aberration. This is important since many electron/ion optical columns are chromatically limited. In the case of very small aberrations, the focused spot size is ultimately limited by the virtual source size multiplied by the magnification of the electron/ion column. Some of the applications that would be helped by better characterized ion beams are, scanning ion microscopy [1], SIMS [2], and microstructure fabrication [3,4].

Measurements of electron energy broadening from a field emitter [5-7] have shown a significantly larger energy spread than predicted by the Fowler-Nordheim theory for field electron emitters alone. This would suggest that additional energy broadening occurs somewhere between the emitter and the image plane of the electron optical system. Since the particles are the most dense and slowest moving within a short distance of the field emitter, this would be the most logical region for additional energy broadening to occur.

In this study, field ion sources will be investigated. In particular, we will be modeling a high brightness Liquid Metal Ion (LMI) source. This source consists of a needle shaped anode on which a liquid metal film flows. The resultant field from a nearby electrode draws the liquid metal up the shank to the high field region of the needle, the apex. At the apex of the needle, there are two competing forces at

work. First there is the surface tension force of the liquid metal, and then there is the force due to the electrical field. The balance of these two forces results in a protrusion on the end of the needle in the shape of a cone [figure 1]. This cone shaped structure was first observed in 1964 by G.I. Taylor [8] while studying the effects of electric fields on soap bubbles and has become known as the Taylor cone. He determined that for a special cone shape, i.e. when the cone half angle was $49.3°$, that the electrostatic and surface tension forces on the cone were in balance. Under the operating conditions of a LMI source, a protrusion has been shown to form on the tip of the Taylor cone [5,9]. The dynamic protrusion becomes elongated with increasing current as shown in figure 2 [9].

The virtual source as seen by the first lens of an electron/ion optical system is defined by projecting the slopes of the trajectories backwards toward the emitter and determining the position where the minimum diameter occurs for these projections. This position is the virtual source position, and the minimum beam diameter d is the virtual source diameter as shown in figure 3. A spherical emitter with particles emitted without transverse energy and with no particle-particle interaction forces will have an infinitely small virtual source diameter whose position will be at the center of the sphere.

Unaccountable increases in both the energy spread and the size of the virtual source have been observed. A 3MeV transmission electron microscope was used to observe an operating LMI source of Gallium [5]. The measurements indicate a physical size of about 15Å in diameter, but various experimental measurements of the virtual source size [11-13] indicate a value between 400 and 1000Å. Again, the most
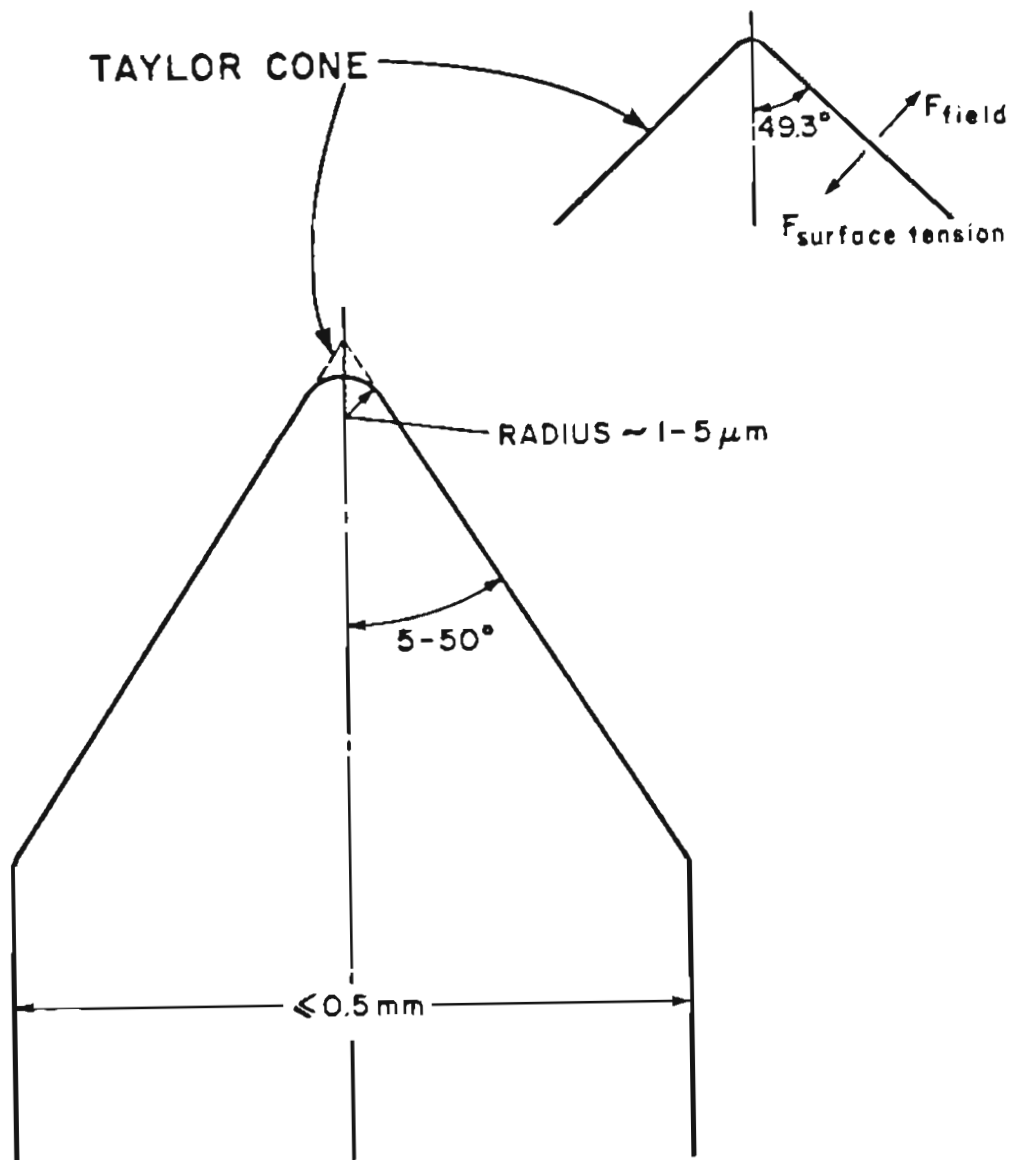
3

TAYLOR CONE

F_{field}

49.3°

$F_{surface\ tension}$

RADIUS ~ 1-5 μm

5-50°

≤ 0.5 mm

Figure 1: Schematic of Taylor cone on needle shaped substrait.

Figure 2: Schematic of Taylor cone with protrusion.

5

VIRTUAL SOURCE
COORDINATES IN
PLANE AT $z = z_0$

$(x_0 y_0)$

x

y

x,y,z
$\dot{x},\dot{y},\dot{z}$

TRAJECTORY

z

Z

SPHERICAL
EMITTING
SURFACE

REFERENCE
PLANE

$$x_0 = x - \frac{\dot{x}}{\dot{z}}(z - z_0)$$
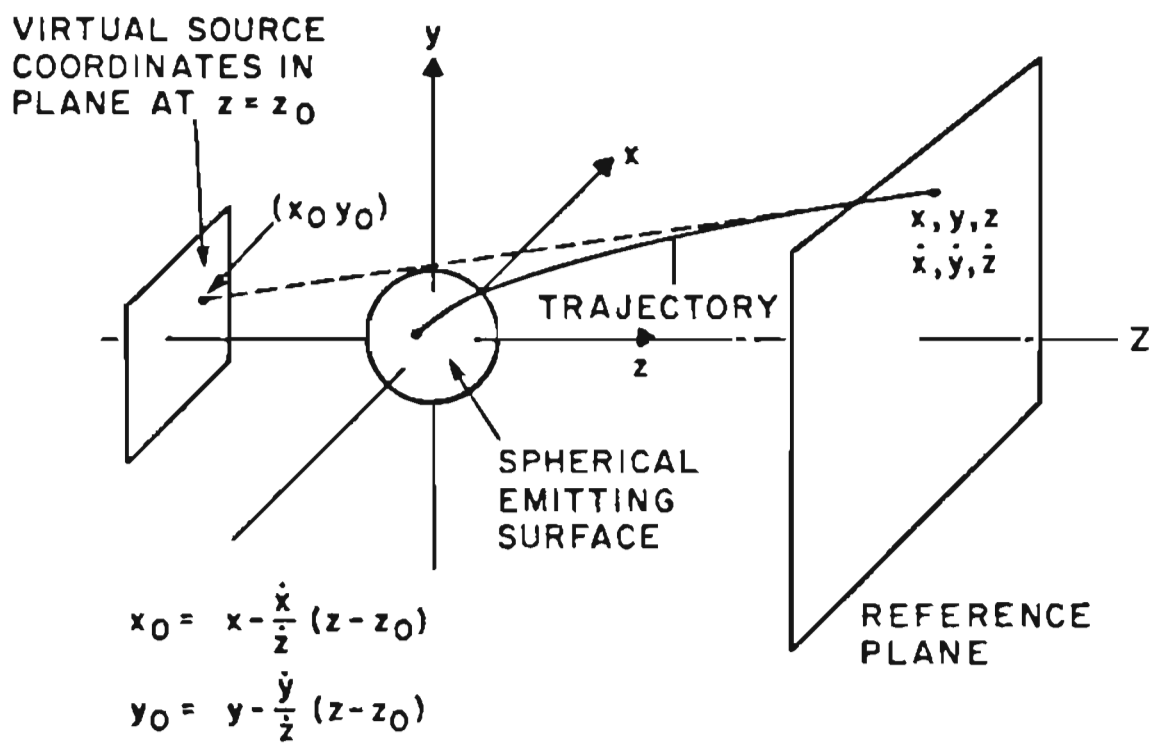
$$y_0 = y - \frac{\dot{y}}{\dot{z}}(z - z_0)$$
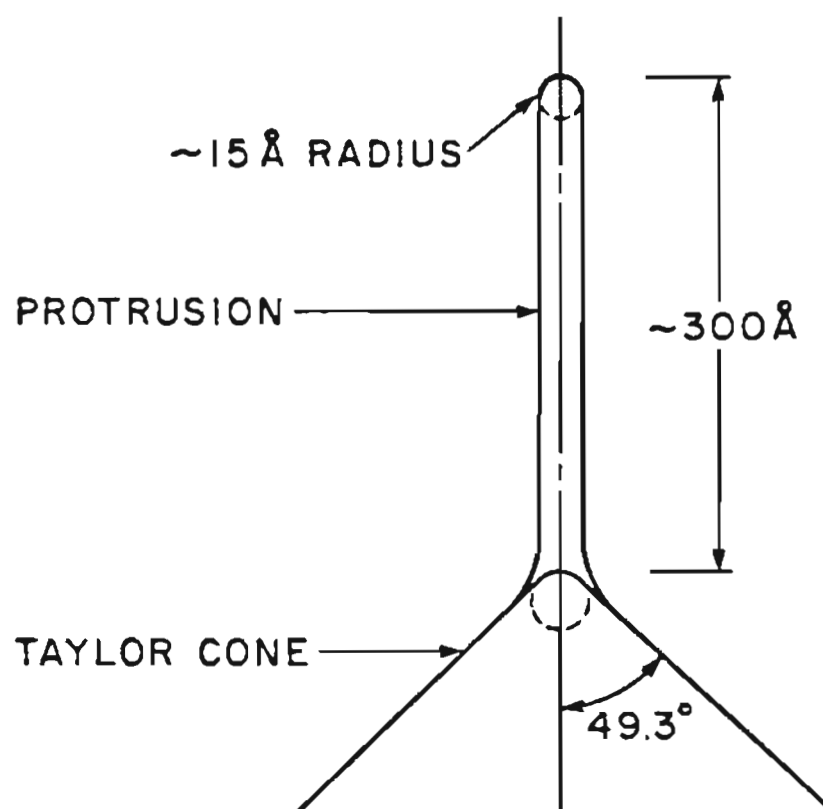
Figure 3: Diagram of the virtual source formation.

likely place for this anomalous expansion of the virtual source is in the vicinity of the emitter, where the particle density is the highest.

Investigations of energy broadening of electron beams began a considerable time ago [14,15], but it wasn't until actual measurements were made by Boersch [16] in 1954 that these energy spreads were linked to the coulomb interaction of the electrons. Thus it has been referred to as the Boersch effect.

Many studies have been carried out on electron beam energy broadening due to the Boersch effect since 1954. Analytical models have been proposed by Loeffler [17], and Zimmermann [18]. Sasaki [19], and El-Kareh and Smithers [20] carried out the first Monte Carlo studies of the energy broadening. Now computer calculations of the space charge and their effects abound [21-32]. Some of these programs have been designed specifically for electron beam lithography or shaped beam applications [33-35].

Since Boersch and later workers considered only electrons, the mass dependence of the energy spread has not been established. Recent experimental investigations using high brightness LMI sources [36-38], show that there is also a mass and charge dependence on the energy spread. This study will show that for a spherical field emitter the energy spread and virtual source size are dependent on current, mass, charge, field strength, emitter radius, emission angle, and total flight distance.

The Monte Carlo program that was used in this study was created by T.R. Groves [39,40] for the study of electrons. Modifications, such as the need for increased accuracy and the ability to vary the mass and the charge of the ions, were required to study the mass and charge characteristics of ions. Other changes

were necessitated due to the low charge to mass ratio of ions, such as the need for increased accuracy and the ability to variable the mass and the change for the ions.

2. Monte Carlo Simulation

A Monte Carlo simulation is a numerical method of modeling a system containing random events. This type of simulation uses a statistically significant number of random events to predict an "average" result. Such simulation models should be compared with experimental data for verification since the results are strongly dependent on the nature of the interaction considered.

Given a choice between an analytical and a numerical solution, the analytic solution will always be preferred because the functional dependence of the experimental parameters is deduced exactly. But in this case, the complexity of the n-bodies interacting with each other precludes the use of an analytical technique. In such a situation the Monte Carlo method [19-21] can be usefully employed. In this Monte Carlo simulation, a random number generator is used to simulate the natural emission process of a field emitter since the field emission process is stochastic in nature. A random number generator is used to initialize the initial position, velocity, and emission time of each ion. At very short but finite time intervals, each ion's position and velocity are updated. The updated position and velocity are determined from the previous position and velocity modified by the coulomb interactions and the local field. After all of the ions have traveled their total flight distance (0.1 mm), each is interrogated for its position and velocity. From all the final positions and velocities, the energy spread and virtual source size are found.

8

The functional dependence of the experimental parameters upon the energy spread and virtual source size can be determined by the repeated running of the simulation, varying one parameter at a time. Each parameter is varied over the entire range of interest so that a complete and accurate functional dependence may be found.

2.1. The Emitter

The emitter is the first place where major concessions had to be made to computer time and space. The shape of the emitter used in this study is not the more realistic Sphere-on-Orthogonal-Cone (SOC) shape [figure 4], but the simpler sphere model [figure 5]. The potential $V(r)$ for a spherical emitter of radius a is

$$V(r) = V_r \frac{Z}{Z-a}\left[1 - \frac{a}{r}\right] \tag{1}$$

where Z is the spacing between the emitter and counter electrode at potential V_r. For the SOC emitter the potential $V(r,\theta)$ is

$$V(r,\theta) = V_r \left(\frac{r_0}{Z}\right)^n \left[\left(\frac{r}{r_0}\right)^n - \left(\frac{r_0}{r}\right)^{n+1}\right] P_n(\cos\theta) - V_{00} \tag{2}$$
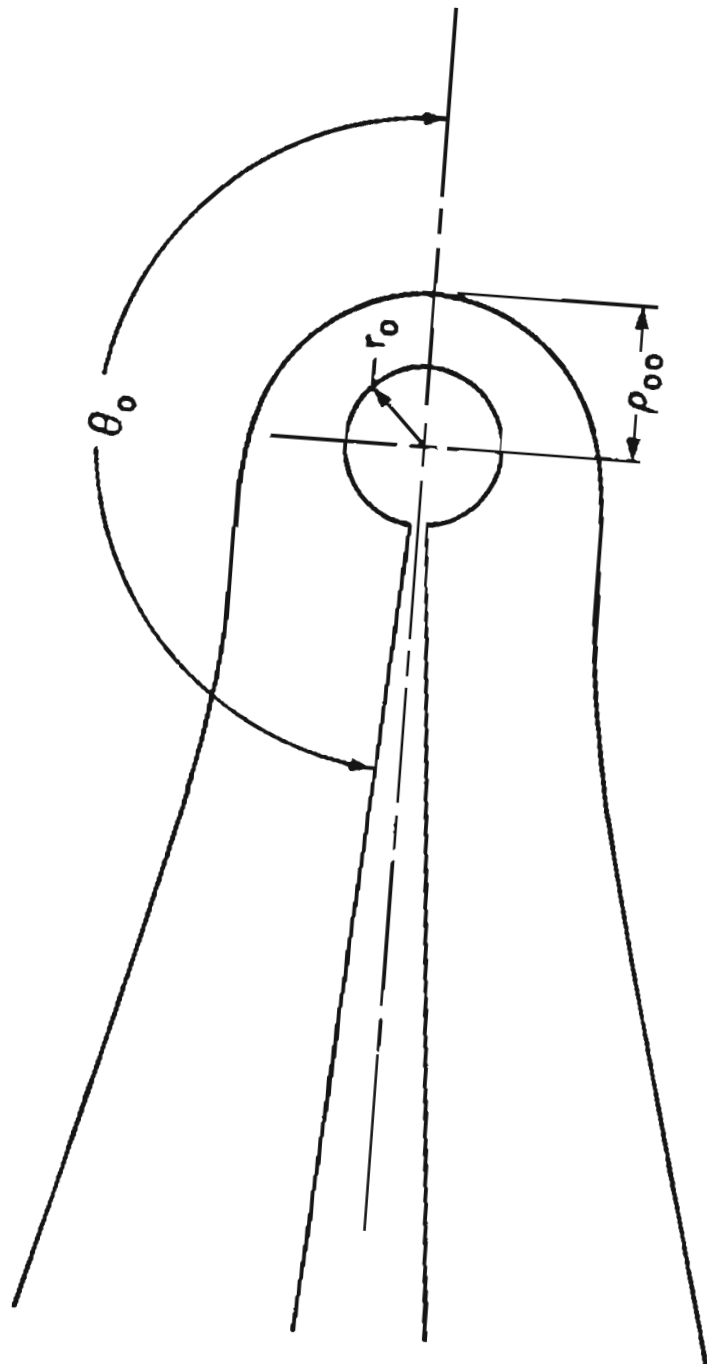
where

$$V_{00} = V_r \left(\frac{r_0}{Z}\right)^n \left[\gamma^n - \gamma^{-n-1}\right] \tag{3}$$

and

$$\gamma = \frac{\rho_{00}}{r_0}$$

The order n of the Legendre polynomial $P_n(\cos\theta)$ is to be take to be 0.5; this yields a 49° half angle cone in accordance with the Taylor cone geometry. Thus the

9

Figure 4: Sphere-on-Orthogonal-Cone and its potential.
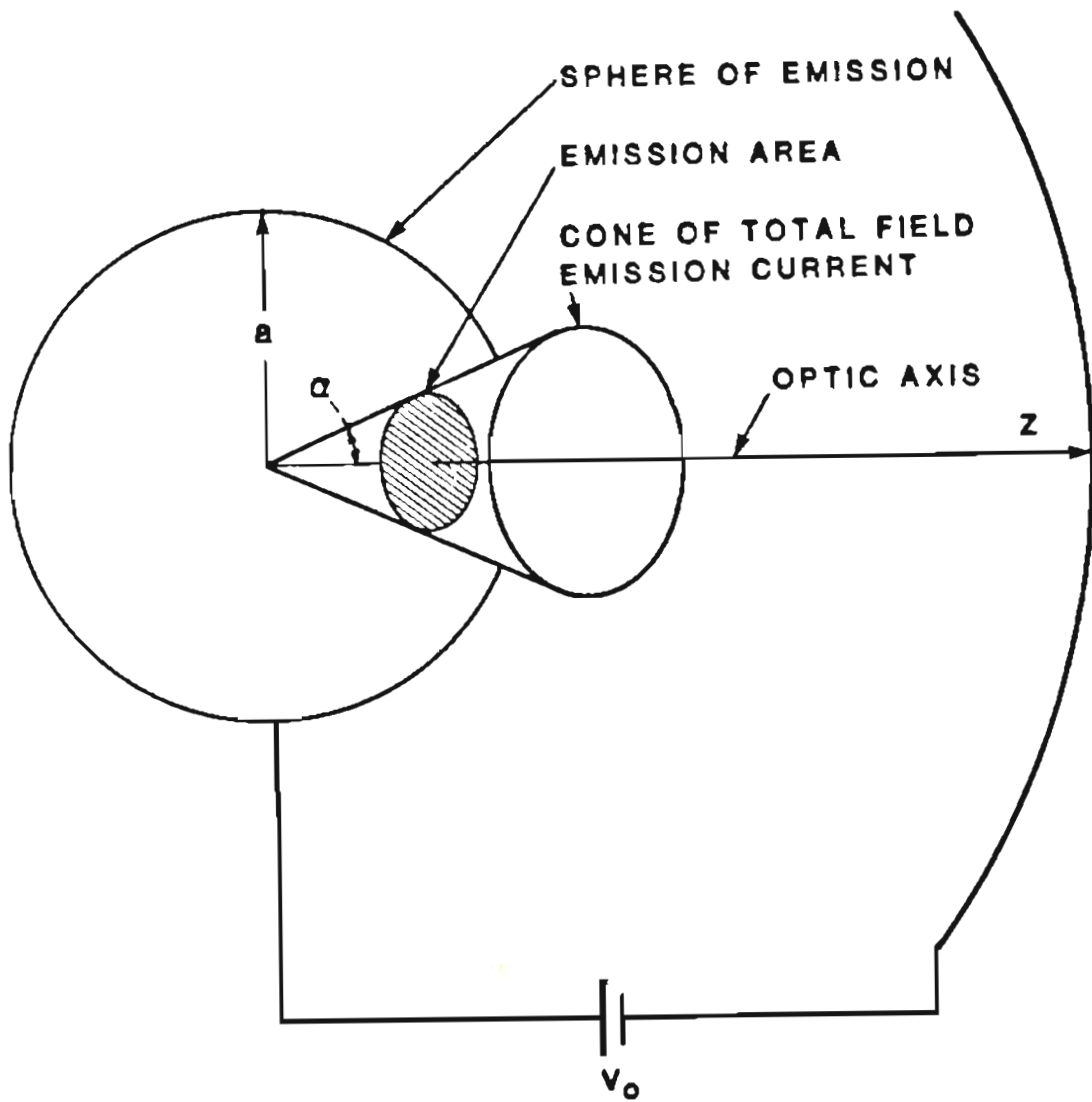
$\gamma \equiv \rho_{00}/r_0$

Figure 5: Schematic of spherical emitter with cone of emission defined.

SOC emitter potential drops off in a more complex fashion than the spherical emitter potential. The reason for the choice of the spherical emitter for this study will be explained in a later section.

Another difference between the simple sphere model and the more realistic SOC model is the fact that the SOC model does not have a constant field strength over its entire surface. When the emission angle θ is increased, a point will be reached where the field strength is insufficient for continued emission. Thus the emission is limited to a cone known as the "cone of emission". Since the sphere does not have any natural limiting feature, one must be imposed. The half-angle of emission α is the imposed parameter. The area of emission is then defined by the area of the surface of the sphere inside a cone whose origin is the center of the sphere with half-angle α [figure 5].

The potential created by the spherical emitter is given by eq(1). The surface field intensity given by $F = V_r/a$ for $Z > a$. The surface field intensity can be changed by adjusting V_r or a. A typical surface field strength for a LMI source assuming field evaporation as the mechanism for ion formation is 2 V/Å.

The next area of interest is the physics of the modeling of the emission process.

2.2. The Emission Process

Firstly, the ions themselves will be treated as point sources of mass and charge. This will not cause a problem since the ions are effectively just that in contrast to an emitter whose size is on the order of 100Å. In the emission process, the ions are assigned positions and velocities. First, the ions are given a position on the

emitting surface from which they are to originate. Secondly, they are given an initial velocity magnitude. Thirdly, they are given an initial direction. And finally, each ion is assigned a "time" of emission. Remembering that this is a Monte Carlo simulation, each of the four previous assignments given to each ion must be random but conforming to certain distribution requirements.

The ions are assigned a point of origination on the emitting surface by a random number generator. These "points of origin" are distributed uniformly over the emitting surface. The particles are assigned Cartesian coordinates as follows

$$
\begin{aligned}
x_j &= R_j \cos\phi_j \sin\theta_j \\
y_j &= R_j \sin\phi_j \sin\theta_j \\
z_j &= R_j \cos\theta_j
\end{aligned}
\tag{4}
$$

where R_j is the randomly generated magnitude of the particles' velocity and ϕ_j and θ_j are randomly generated polar coordinates. For the case of the particles launched with finite initial velocity, randomized emission directions are also produced by the program. The initial velocity is simply added vectorially to the velocity of the particle that is derived from the field. A finite transverse velocity causes the emission to move off the surface normal. This is ultimately reflected in a finite virtual source size, even for the case of no particle-particle interaction. As can be seen in figure 6, the virtual source size d caused by a transverse component of the initial velocity is [41]

$$
d = a \left(\frac{V_t}{V_r} \right)^{1/2}
\tag{5}
$$

where $V_t \equiv$ transverse energy and $V_r \equiv$ applied potential. In the next section it will be shown that the value of d calculated by equation (5) compare favorably with
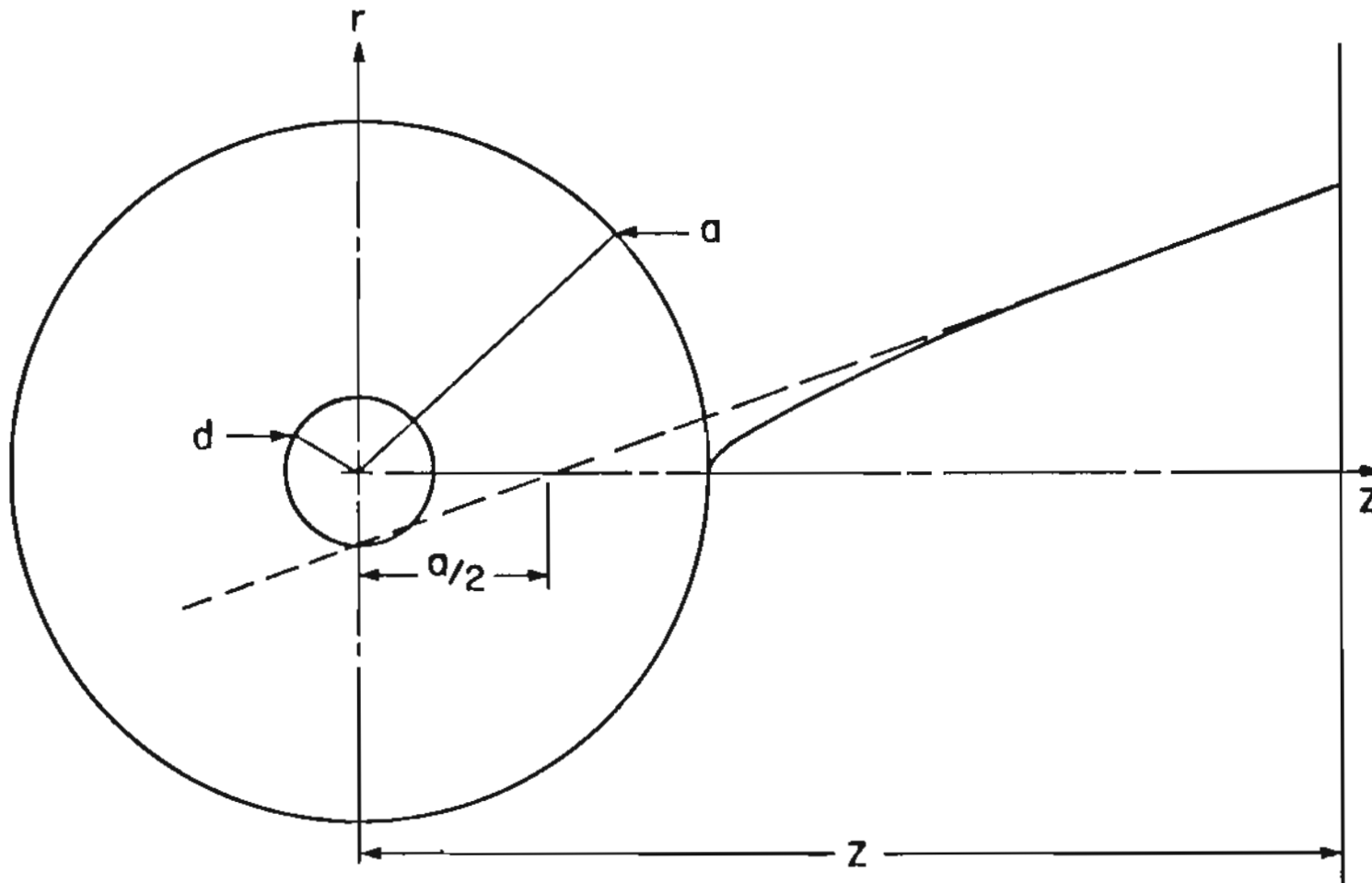
Figure 6: Schematic of an emission from a sphere and the virtual source formation due to the non-zero transverse velocity.

the virtual source diameter calculated by the program. For the case of the ions launched "cold" (i.e. with zero initial velocity), the direction of emission is simply normal to the surface at the point of emission and $d = 0$.

In the field emission process the emitted particles posses an energy distribution. The energy distribution for an LMI source is not known, thus we employ the energy distribution used by Groves [40], namely

$$N(E) = \frac{1}{E_0} e^{-E/E_0} \tag{6}$$

where $N(E)dE$ is the probability of observing a particle with kinetic energy between E and $E+dE$, and E_0 is the width of the distribution. Since we want to assign a random energy modified by equation (6) to each particle, there is a further problem. The random number generator gives us a random number X which is distributed uniformly between zero and one. Where as we want the random number distributed over a different range and a different distribution. The following theorem provides a way of doing this.

Theorem: Given a random number X, uniformly distributed between zero and one, we wish to generate a number Y, distribution according to the known distribution $N(Y)$. A functional relationship $Y(X)$ exists, and is given by

$$Y = f^{-1}(X)$$

where f^{-1} is the inverse of the function f defined by

$$f(Y) = \int_{Y}^{Y_0} N(Y) \, dY$$

Following Groves [40] Y_0 is defined by $Y_0 = Y(0)$, and $N(Y)$ is normalized so that

$$\int_{Y(1)}^{Y(0)} N(Y) \, dY = 1$$

The variable Y can represent any physical quantity which is distributed according

to a known law. The theorem is therefore quite general, and its proof is shown in Appendix A.

To show the usefulness of the above theorem, we will use it to derive the equation necessary for creating the distribution for equation (6). Starting with equation (6),

$$N(Y) = \frac{1}{E_0} e^{-Y/E_0}$$

Assuming $Y(0) = 0$, we find

$$f(Y) = \frac{1}{E_0} \int_Y^0 e^{-Y/E_0} dY = 1 - e^{-Y/E_0}.$$

By setting $X = f(Y)$ and inverting, we get

$$Y = f^{-1}(X)$$

or

$$E = -E_0 \ln(1 - X) \tag{7}$$

where $E \equiv Y$ and E is the random energy of the electron determined from the computer generated, uniformly distributed, random number X.

Once given an initial energy, the particle is given a random emission direction. Again, following Groves [40] we assume that the distribution is Lambertian, i.e.,

$$\frac{dI}{d\Omega} = \frac{\cos\theta'}{\pi} \tag{8}$$

where $dI/d\Omega$ is the current per unit solid angle, and θ' is the angle measured relative to the local normal to the surface. In terms of θ' the distribution is

$$\frac{dI}{d\theta} = N(\theta') = 2\sin\theta'\cos\theta'.$$

By applying the preceding theorem to generate the randomized angle θ_j, for the jth

particle, from the uniformly distributed random number X, the following equation is found

$$\theta_j' = \sin^{-1}\sqrt{X}$$

The local azimuth ϕ_j' can be generated as above, where $\phi_j' = 2\pi X$.

The velocity components in Cartesian coordinates are as follows

$$v_{xj}' = v_j \cos\phi_j' \sin\theta_j'$$
$$v_{yj}' = v_j \sin\phi_j' \sin\theta_j'$$
$$v_{zj}' = v_j \cos\theta_j'$$

Now $\vec{v}'$ must be rotated into the appropriate local coordinate system (figure 7). Two rotations are necessary. A rotation through θ_j (about the z-axis), then another rotation through θ_j (about the y-axis) is performed. The velocity is now in the proper orientation for which a Lambertian distribution about the local normal exists. The true velocity $\vec{v}$ is then given by

$$
\begin{pmatrix} v_x \\ v_y \\ v_z \end{pmatrix} =
\begin{pmatrix} \cos\theta & 0 & -\sin\theta \\ 0 & 1 & 0 \\ -\sin\theta & 0 & \cos\theta \end{pmatrix}
\begin{pmatrix} \cos\phi & -\sin\phi & 0 \\ \sin\phi & \cos\phi & 0 \\ 0 & 0 & 1 \end{pmatrix}
\begin{pmatrix} v_x' \\ v_y' \\ v_z' \end{pmatrix}
$$

where the subscript j labeling each particle is omitted for simplicity.

Finally, the most important random initializing variable is the emission time. The ions must be emitted randomly but they must also be consistent with the desired total field emission current. The current I due to the emission of n ions is:

$$I = qn/T \tag{9}$$

where q is the charge per particle (assuming that all of the particles have the same charge), and T is the emission time (i.e., the time in which all of the particles must be emitted). Therefore, for a given q and n, the emission time is determined by I.
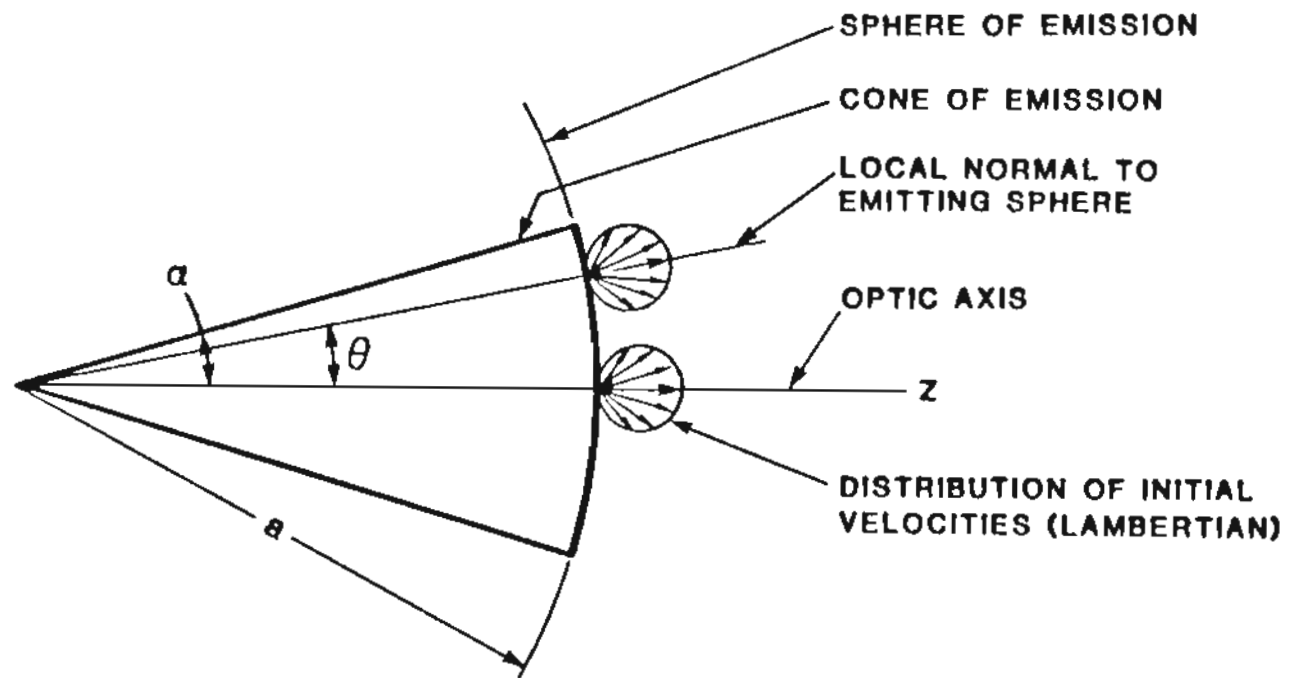
Figure 7: Diagram showing the initial emission position and direction.

Since the emission process is assumed to exhibit full shot noise, the emitted particles are expected to follow a Poisson distribution in time.

In this simulation, the particles are allowed to travel without any outside influences for a very small but finite amount of time (Δt) between interactions. Using a sufficiently small Δt, the real case of a continuous modification of the particles trajectories can be more closely approached. This brings us to a problem mentioned by Groves [39]. If one were to simply determine which of the ions will be launched within each time interval Δt and launch them from the surface of the emitter at the beginning of each time interval, then the emission would be "bunched." This is shown schematically in figure 8(a). This problem is particularly acute when the average time between emission events $<t> = q/I$ is small compared to Δt. That is when $I > q/\Delta t$. What is needed in this situation is a "debunching" scheme. The debunching is achieved by first, determining within which time interval each emission will occur, then, instead of launching the ions from the emitter surface, the program simply distributes them randomly in the space corresponding to the time interval Δt. Thus, the particles are effectively "created" a certain distance from the emitter and the particles are "debunched as shown schematically in figure 8(b). But since 10,000 steps were used in our case, this bunching problem only existed in the extreme of high current and large particle mass. The question arises, "Can the ions be created a short distance from the emitter and not affect the final result? After all, the area close to the emitter is the crucial area. It is here that the particles are moving the slowest, and the current density is the highest." The answer is yes. The ions can be created a short distance from the emitter with little

CORRECTION OF BUNCHING ERROR
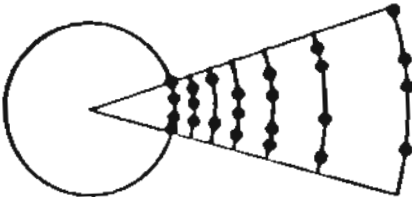
WITH BUNCHING
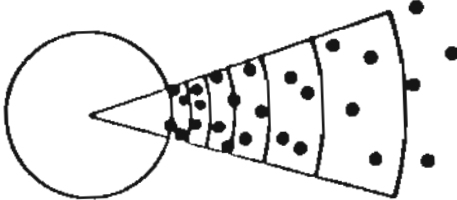
BUNCHING CORRECTED

Figure 8: Schematic of spatial bunching of emission (a) and removal of bunching (b).

deviation from reality for a number of reasons. First, in the field evaporation process, the ions are not created at the surface, rather, they are created a short distance from the emitter surface due to the quantum mechanical tunneling process. Secondly, since the ions are moving their slowest in this area, the distance moved during Δt is also at its smallest. And lastly, even though the current density is at its highest, the average distance away from the emitter in which these particles are created is small. Let us calculate this distance for the standard conditions. The force is:

$$f = eE = (1.602 \times 10^{-19} C)(2.0 \times 10^{10} V/m) = 3.204 \times 10^{-9} \text{ N} \tag{10}$$

The acceleration of a one amu particle with the above force is:

$$a = \frac{f}{mass} = \frac{3.204 \times 10^{-9} \text{ N}}{1.637 \times 10^{-27} \text{ kg}} = 1.9572 \times 10^{18} \text{ m/sec}^2 \tag{11}$$

The velocity of this particle at the end of the time used in our case $\Delta t = 3.58 \times 10^{-14}$ sec is:

$$v_1 = v_0 + a_0(\Delta t) = 7.320 \times 10^4 \text{ m/sec} \tag{12}$$

Where v_0 is the initial velocity of a one amu particle given 0.1 eV of energy. The total distance traveled by this particle in time Δt is:

$$d = v_1(\Delta t) = 2.520 \times 10^{-9} \text{ m} = 25\text{Å}. \tag{13}$$

The average distance from the surface that a particle is created is $\frac{1}{2}$ of the total distance that the particle travels in time Δt. Therefore the average distance of creation is 12.5Å, or one sixteenth the tip radius. We must also remember that in this simulation the particles travel unaffected by any forces during the time intervals Δt. It is only in using small enough time intervals that we gain an accurate approximation of not only the emission of the particles, but the rest of the flight as

well. But how small must Δt be in order that the simulation be accurate? This question that will be left to the next section: Determining the Trajectories.

2.3. Determining the Trajectories

Now that the emitter and its field are described and the emission process is characterized, let us examine the ion trajectories. The trajectories will be followed from the origin to a "reference plane" where their positions and velocities are recorded. Each ion will feel forces from the applied field, from the other ions, and from the image charges inside the emitter.

We must now determine just how this calculation will be made. A straight forward update of the position and velocity can be found from the previous position, velocity, and acceleration as shown below

$$\vec{v}_{i+1} = \vec{v}_i + \vec{a}_i \Delta t \tag{14}$$

$$\vec{r}_{i+1} = \vec{r}_i + \vec{v}_{i+1} \Delta t \tag{15}$$

(The reason for using $\vec{v}_{i+1}$ rather than v_i in the calculation of $\vec{r}_{i+1}$ can be found in reference 42.)

By a simple calculation we can determine just how many iterations would be required for an accuracy of 1% of $v\Delta t$ for the first step. The leading error term in equation (16) is

$$\text{Error} = \frac{1}{2} a (\Delta t)^2 \tag{16}$$

For an error of less than or equal to 1% of $v\Delta t$ we have

$$\frac{1}{2} a (\Delta t)^2 \leq (.01) v (\Delta t) \tag{17}$$

or

$$\Delta t \leq \frac{(.02)v}{a} = 7.480\times10^{-16}\text{sec} \tag{18}$$

For a total flight distance of 100 μm, the total flight time is 3.580×10^{-10} sec for 1 amu, thus requiring 5×10^5 iterations. Clearly a more efficient algorithm must be found. The program in our case was run for as many as 10^4 steps but it is totally impractical to try to run the program for 50 times that many steps.

Two frequently used methods of numerical integration are the Runge Kutta method or Hamming's predictor-corrector method [43,44]. Of these two methods, Hamming's predictor-corrector method is the most efficient, but it does have some drawbacks. The predictor-corrector methods requires the knowledge of four equally spaced positions and their corresponding velocities. By using four positions, a fifth position can be predicted. By using the predicted position and the differential equations, the new position is corrected. The need for four previous positions means that this method is not "self-starting". Another method must be used to provide the first four positions before this method can be started. The need for equally spaced positions means that it is difficult to change from a place where a high density of positions is needed to a place where a lower density of positions is sufficient. The Runge Kutta method is slower, but has the advantage of being both self-starting and each new position calculated does not need to be spaced the same as its predecessors. So, when more accurate (or less accurate) calculations are needed, it is easy to make smaller (or larger) steps. In many cases both of these methods are used in conjunction. The Runge Kutta method is used to start the calculations and to adjust the accuracy. If accuracy were more important in a certain region, the step size could be adjusted and only the first four positions in the new region could be determined

by the Runge Kutta method and the more efficient predictor-corrector method would be used for the remaining calculations.

To judge the accuracy of Hamming's numerical method, Groves [39], using electrons, assumed no mutual interactions and compared the results to the analytic solution. He found that for 800 steps, the answers were considerably different for an emitter to anode distance of 0.1mm. This is because each error that is incurred, is used in the calculation of the next value, that is, the errors are additive. In the above case, an electron was followed to a distance of 2.6 μm (10 tip radii) where the difference between the analytical solution and the numerical solution was found to be 219 eV! Since this was an unacceptably large error, Groves used a combination of the analytic and numeric solution. In the absence of interactions among the particles, the particle trajectories are easily described by the Rutherford central force scattering.

The equations of motion for a concentric sphere system in polar coordinated are as follows:

$$\ddot{r} - \frac{k}{r^2} - \frac{L^2}{r^3} = 0 \tag{19}$$

$$\frac{d}{dt}(r^2\dot{\theta}) = 0 \tag{20}$$

where

$$k = \frac{-eaV_0}{m} \tag{21}$$

where $k>0$ since $V_0<0$, and

$$L = r_0^2\dot{\theta}_0 \tag{22}$$

where (mL) is the initial angular momentum.

The first integrals of the velocity components are easily obtained, they are:

$$\dot{r} = \left[\dot{r_0^2} + 2k\left[\frac{1}{r_0} - \frac{1}{r}\right] + L^2\left[\frac{1}{r_0^2} - \frac{1}{r^2}\right]\right]^{1/2} \tag{23}$$

where the zero subscript refers to the initial value, and

$$\dot{\theta} = \frac{L}{r^2} \tag{24}$$

The second integral for $r(\theta)$ is familiar, and can be found in many books.

The above description is only in two-dimensions, and as such, creates certain problems when placing it in three-dimensional space. One problem is that when using the above equations in spherical coordinates, there are discontinuities in the angular coordinates across certain boundaries. To circumvent this problem, Groves carried out the calculations in cartesian coordinates.

The above equations in cartesian coordinates written in terms of the coordinates of x_i are as follows:

$$v_i = \frac{L_j - L_k}{x_i + x_j + x_k} + \frac{x_i}{r^2}\left[L_i + L_j + L_k + r\dot{r}\right] - \frac{2x_i}{r^2}\frac{x_iL_j + x_jL_k + x_kL_i}{x_i + x_j + x_k} \tag{25}$$

and

$$r^2 = \sum_i^N x_i^2 \tag{26}$$

where (i,j,k) refer to all cyclic permutations of the components (x,y,z), and mL_i are the conserved components of angular momentum given by

$$L_i = x_{j0}v_{k0} - x_{k0}v_{j0} \tag{27}$$

In order to reduce the error in the predictor corrector method, both the numeric and analytic solutions of the equations of motion were solved simultane-

ously without interaction. The numerical solution and the analytical solution were compared after each step, and the correction term $\delta\vec{v}$ was saved for later use. This means that for a given set of values of $\vec{r}_0$ and $\vec{v}_0$ at the beginning of any time interval Δt, the computer numerically computes the values of $\vec{r}$ and $\vec{v}$ for the end of the time interval. Using the computed value of $\vec{r}$, we can then find what the value of $\vec{v}$ should be, by using the analytic formula.

Next the simulation was rerun using the particle interactions. It is here that the saved values of the velocity error $\delta\vec{v}$ due to the numerical integration techniques were used. We note that $\delta\vec{v} = \vec{v}_n - \vec{v}_a$, where $\vec{v}_n$ is the numerically calculated velocity and $\vec{v}_a$ is the analytically calculated velocity. The numerically calculated velocity which includes particle interaction $\vec{v}_{in}$ was modified by the velocity error $\delta\vec{v}$ to obtain a more correct value for $\vec{v}_{in}$. That is, $\vec{v}_{in}' = \vec{v}_{in} - \delta\vec{v}$. This effectively corrects the discretization error whose contribution is from the spherical accelerating field without affecting the contributions due to particle interactions.

The effectiveness of this approach can be seen by comparing Table I with Table II. One can see how bad the numerical approach is alone. Table II, in the absence of the particle interaction effects, has a discretization error after 20 steps reduced to eight thousandths of an electron volt where Table I has an error of 0.1eV for the same distance. One tenth of an electron volt is a large error considering that it has traveled only 0.5% of the total number of steps that it must travel. The same test was run for the virtual source size calculation. By removing the Lambertian distribution of initial velocities, mutual interaction effects, and using only cold ions, the virtual source size was 3×10^{-22} Å using a value of $\Delta t = 8.94\times10^{-14}$ sec,

Table I: A comparison of the numeric and analytic values of the kinetic energy is shown. All standard input parameters (see Table III) apply. Equation 14 and 15 are used to calculate the first 20 of 4000 steps. Mutual interactions are excluded.

A Simple Trajectory Computation			
no mutual interactions, no feedback correction			
step	r (meters)	kinetic energy eV (numerical)	kinetic energy eV (analytical)
1	0.802E-7	0.302062E+3	0.301938E+3
2	0.950E-7	0.317325E+3	0.317217E+3
3	0.120E-6	0.334539E+3	0.334426E+3
4	0.132E-6	0.340421E+3	0.340321E+3
5	0.154E-6	0.348918E+3	0.348818E+3
6	0.176E-6	0.355447E+3	0.355347E+3
7	0.200E-6	0.360805E+3	0.360705E+3
8	0.223E-6	0.364949E+3	0.364849E+3
9	0.247E-6	0.368322E+3	0.368222E+3
10	0.271E-6	0.371105E+3	0.371005E+3
11	0.295E-6	0.373453E+3	0.373353E+3
12	0.318E-6	0.375455E+3	0.375355E+3
13	0.342E-6	0.377183E+3	0.377083E+3
14	0.366E-6	0.378688E+3	0.378588E+3
15	0.390E-6	0.380011E+3	0.379911E+3
16	0.414E-6	0.381183E+3	0.381083E+3
17	0.438E-6	0.382227E+3	0.382127E+3
18	0.462E-6	0.383164E+3	0.383064E+3
19	0.487E-6	0.384009E+3	0.383909E+3
20	0.511E-6	0.384775E+3	0.384674E+3

Table II: This table shows the accuracy of the numerical technique with the feedback correction. In this the case, the standard input parameters (see Table III) are used. The first 20 of 4000 steps are shown. Again, mutual interaction terms are excluded.

Improved Trajectory Computation feedback correction but no mutual forces			
step	r (meters)	kinetic energy eV (numerical)	kinetic energy eV (analytic)
1	0.802E-7	0.301934E+3	0.301934E+3
2	0.950E-7	0.317211E+3	0.317211E+3
3	0.120E-6	0.334420E+3	0.334420E+3
4	0.132E-6	0.340314E+3	0.340314E+3
5	0.154E-6	0.348811E+3	0.348811E+3
6	0.176E-6	0.355341E+3	0.355341E+3
7	0.200E-6	0.360700E+3	0.360700E+3
8	0.223E-6	0.364844E+3	0.364844E+3
9	0.247E-6	0.368218E+3	0.369218E+3
10	0.271E-6	0.371002E+3	0.371001E+3
11	0.295E-6	0.373350E+3	0.373349E+3
12	0.318E-6	0.375353E+3	0.375352E+3
13	0.342E-6	0.377082E+3	0.377080E+3
14	0.366E-6	0.388588E+3	0.378585E+3
15	0.390E-6	0.379912E+3	0.379908E+3
16	0.414E-6	0.381084E+3	0.381080E+3
17	0.438E-6	0.382130E+3	0.382125E+3
18	0.462E-6	0.383067E+3	0.382125E+3
19	0.487E-6	0.383913E+3	0.383906E+3
20	0.511E-6	0.384680E+3	0.384672E+3

a = 200Å, F = 2 V/Å, m = 1 amu, n = 120 particles. This shows that the value of Δt is sufficiently small for this case. It would be one order of magnitude smaller had we not used the combined numerical and analytical techniques.

Another way to show that the virtual source size is a reasonable value is to compare it to the analytical results of equation (5). For the standard input parameters (initial transverse potential V_t = 0.1 eV, i.e., assuming 100% of the initial kinetic energy is transverse, M = 1 amu, l = 1 μm applied potential V_r = 400V, and emitter radius a = 200Å) we find from equation (5) that d = 3.16Å. Therefore, the value of the numerically calculated virtual source diameter (d) should be less than 3.16Å. This is because not all of the initial kinetic energy is in a transverse direction. The program was run for the standard input conditions without the particle-particle interaction term and $\Delta t = 8.94 \times 10^{-14}$ sec, n = 120 particles, and N = 10,000 steps. The value of the virtual source diameter was found to be 2.2Å. Therefore, the virtual source size from the numerical calculation is reasonable.

There is an additional benefit by using time rather than distance as the parameter of movement. This is because, when time is used as the stepping parameter, the distance traveled by any one ion in the time Δt is dependent on v_i and a_i (and is therefore dependent on distance from the emitter, since a_i decreases with distance). When a particle is in the vicinity of the emitter, it is important that Δr_i be as small as possible, since it is here that the field and hence a_i is changing most rapidly with distance.

Recalling that the Hamming predictor-corrector method requires four initial positions to start, it is necessary to find a way of determining the first four positions

of the emitted ions. Rather than use the Runge Kutta method, we follow Groves by using the initial position of each particle and calculating a "previous" position by stepping backwards in time. This process was repeated two more times. Although some of these previous positions may find themselves in the unreal situation of existing a distance inside the emitter, no problems are caused because the program does not check for boundary condition violations and treats these positions like any other. The acceleration was set to zero during the back-stepping since acceleration at those points caused backward projections that curl.

Hamming's predictor-corrector method is applicable to first order differential equations of the general form: $y'=f(x,y,y')$. Equations of motion must be decomposed into a set of coupled first order differential equations as follows:

$$\frac{d\vec{r}_j}{dt} = \vec{v}_j \tag{28}$$

and

$$\frac{d\vec{v}_j}{dt} = \frac{\vec{f}_j}{m} \tag{29}$$

where $\vec{f}_j$ is the net force on the jth particle. In the program by Groves the force $\vec{f}$ was separated into three major components:

1. The spherical accelerating field;

2. The coulomb force on every ion due to every other emitted ion in the sample;

3. And the coulomb force on every ion due to the image charges of every emitted ion (including the ion of interest).

The total force $\vec{f_j}$ is given by

$$\vec{f_j} = qV_0R_0\frac{\vec{r_j}}{|\vec{r_j}|^3} + \frac{q^2}{4\pi\epsilon_0}\sum_{k=1,k\neq j}^{N}\frac{\vec{r_j}-\vec{r_k}}{|\vec{r_j}-\vec{r_k}|^3} + \frac{q^2}{4\pi\epsilon_0}\sum_{k=1}^{N}\lambda_k\frac{\lambda_k\vec{r_k}-\vec{r_j}}{|\lambda_k\vec{r_k}-\vec{r_j}|^3} \qquad (30)$$

where $\lambda_k=R_0/|\vec{r_k}|$. The three contributions are represented in the same order as introduced. Notice that the image force is always attractive. The image charge of the kth ion is $\lambda_k q$, and its position is $\lambda_k\vec{r_k}$. As $\vec{r_k}$ becomes greater, the image charge moves toward the center of the sphere, diminishing in magnitude as it goes. Two contributions have been omitted in equation (30), these are the magnetic forces between the moving ions, and the radiation damping due to the accelerating ions. Both of these were neglected.

Since $\vec{f_j}$ contains terms which depend only on the ion coordinates, the first order equations of motion are of the form required by Hamming's method. We have 6 n coupled equations for n particles and these must be solved simultaneously, which is no problem for a fast computer.

When running this program, there are several non-experimental parameters which need to be adjusted. These are parameters which arise from the fact that this simulation is numerical in nature and computers have inherent resource limitations. The parameter which is introduced because of the numerical nature of the simulation is Δt, or the step time. The step time is decreased by increasing the number of steps N . The number of steps must be increased until a point is reached where additional increases cause no significant change in the resultant energy spread or virtual source size as illustrated in figure 9. In figure 9 we see that 4000 steps was a sufficient number. So why was 10,000 steps used? Early in the
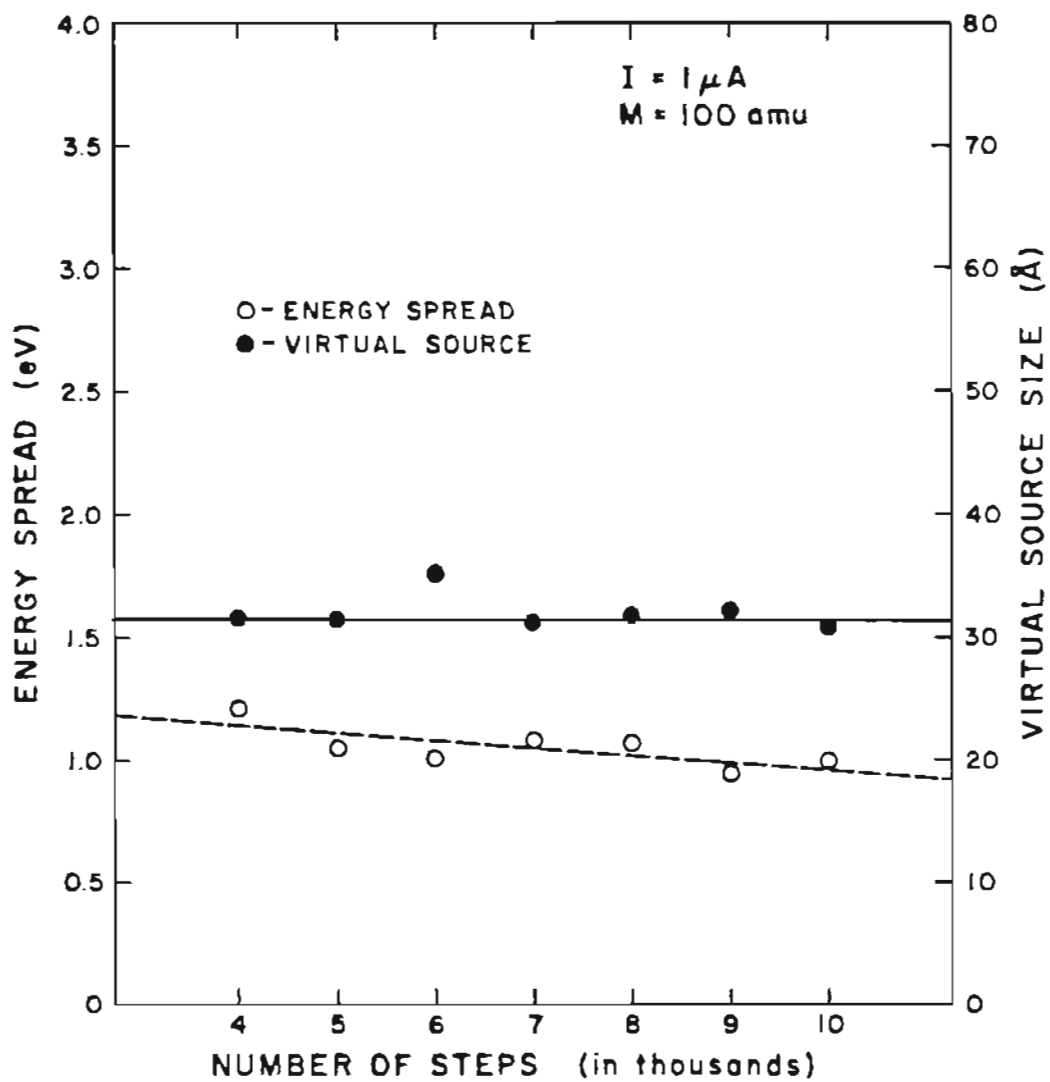
Figure 9: Energy Spread and Virtual Source Size vs. Number of Steps.

project while a different method of calculating the virtual source size was used, 9000 steps were required to reach a constant result, owing to the fact that the previous method of calculating virtual source size was not as appropriate as the one used here (and described in a later section). When the new method was first used, the number of steps required for a constant result was not reinvestigated immediately. It was later determined that the number of steps was an over-kill, but for reasons of consistency, the 10,000 steps were used for the remainder of the calculations. By running the program for such a large number of steps, we can be assured that the number of steps does not influence the final results.

The other non-experimental parameter which required adjustment was the number of emitted ions, n. If computer time and memory were no object, the minimum number of particles launched would be enough to entirely fill the electrode space. That means by the time the first particle reaches the reference plane, the last particle would be just emitted (i.e., the emission time T is greater than or equal to the total flight time t). What this condition means in terms of the current is:

$$I \leq 2.2 \times 10^{-15} \left[\frac{qFa}{M} \right]^{1/2} \frac{n}{Z} \qquad (31)$$

Where $F \equiv$ field strength in V/Å; $a \equiv$ tip radius in Å; $M \equiv$ mass in amu; $q \equiv$ charge in units of 1.6×10^{-19} coul.; $n \equiv$ number of ions; and $Z \equiv$ the total flight distance. A quick calculation using the standard values for the parameters as found in Table III, shows that there are not nearly enough particles to fill the diode space for a spacing of $Z = 0.1$mm. In fact, we happen to be short a quite a few particles, about two orders of magnitude! And the possibility of "end effects" is real. Thus, in the diode, we have a "packet" of particles as shown schematically in figure 10. One
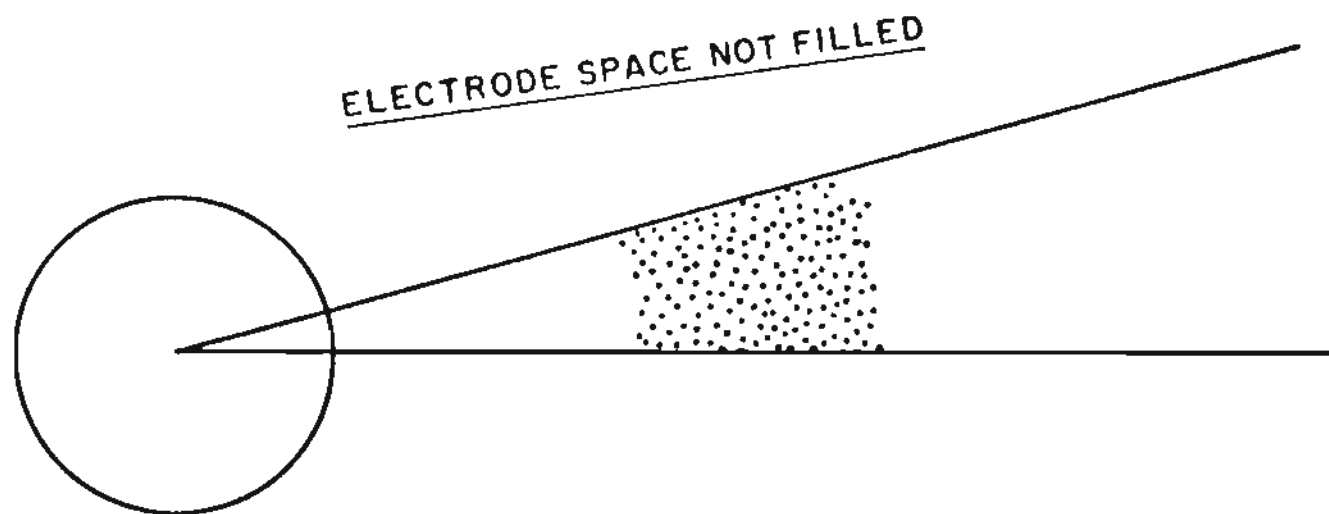
ELECTRODE SPACE NOT FILLED

Figure 10: Packet of particles traveling between electrodes.

way to show empirically that these "end effects" are not significant, is to show that by increasing the number of particles the final result does not change. This was found to be the case as seen in figure 11, for the energy spread and virtual source size for the standard input parameters. But what about the worst case of $1\mu A$ of current and 100 amu particles? In figure 12 the virtual source size for $M = 100$ amu shows an overall increase with n. But by plotting the virtual source size vs. mass at $n = 120$ (figure 13) one observes that the result at $M = 100$ amu (figure 12) is only slightly above the regression line. This is the only instance where we found the number of particles to be insufficient. It would have taken a significantly longer CPU time for each run if 160 particles were used instead of the 120 (computation time increases as n^2).

Table III: The standard values of the input parameters.

Standard Values
$I = 1\ \mu A$
$M = 1$ amu
$q = 1.602 \times 10^{-19} C$
$a = 200\ \text{Å}$
$F = 2\ V/\text{Å}$
$Z = 100\ \mu m$
$\alpha = 0.3$ rad
$n = 120$ particles
$N = 10,000$ steps
$\Delta E_i = 0.0$ eV
$E_i = 0.1$ eV

Another way to show that the lack of sufficient particles to fill the electrode space is not cause for alarm is by looking at a graph of particle energy in the reference plane vs. emission order. If these end effects were significant, the particles in
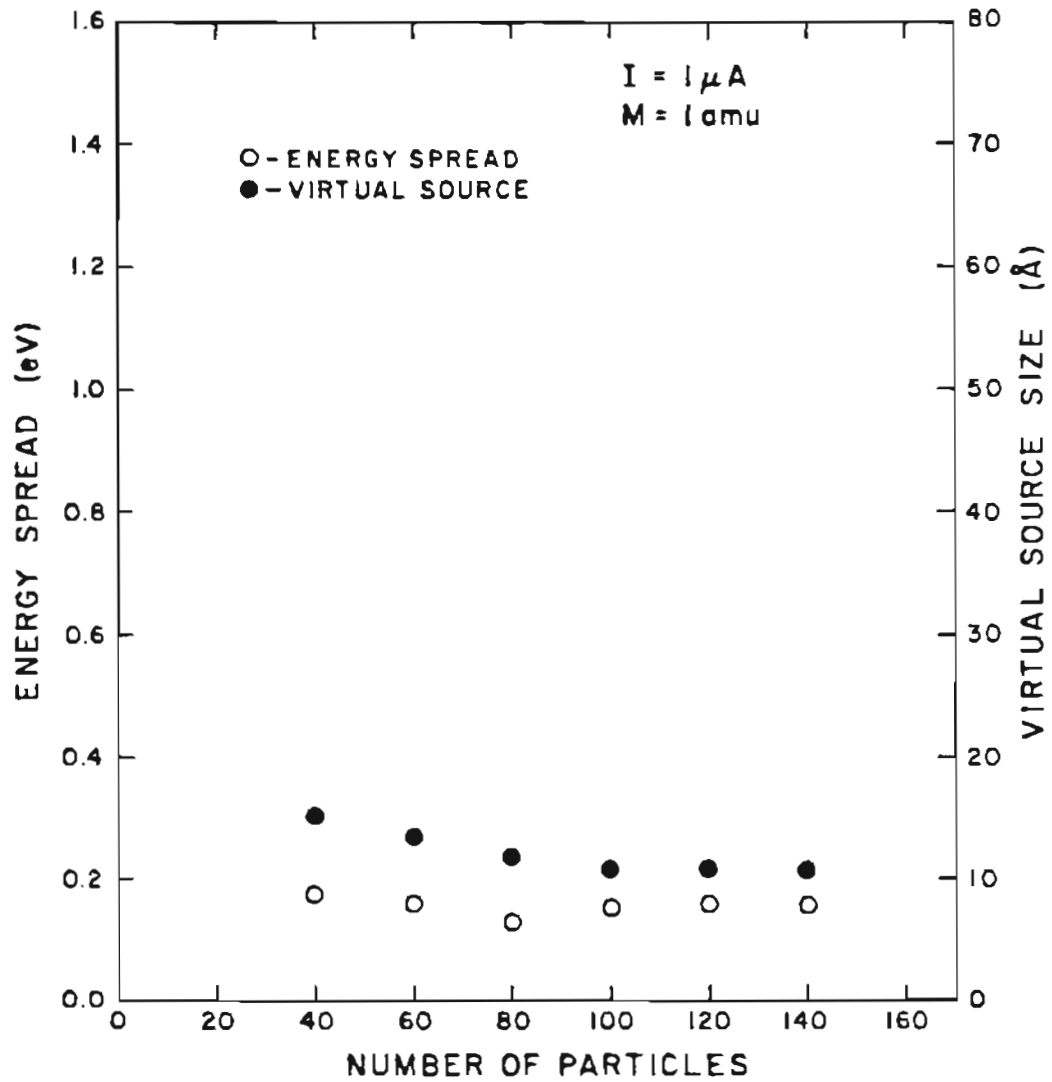
Figure 11: Energy Spread and Virtual Source Size vs. Number of Particles (using the standard input parameters, see Table III).
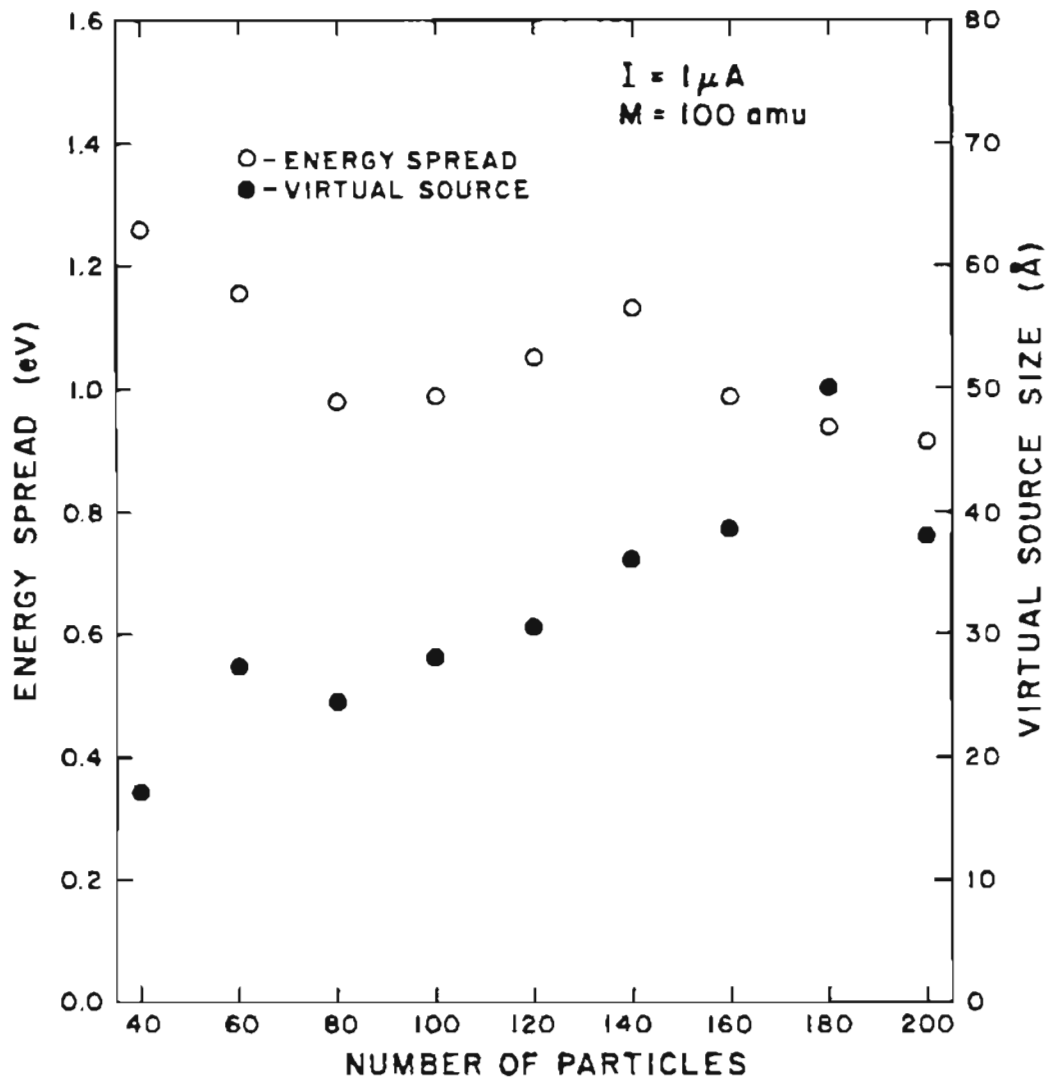
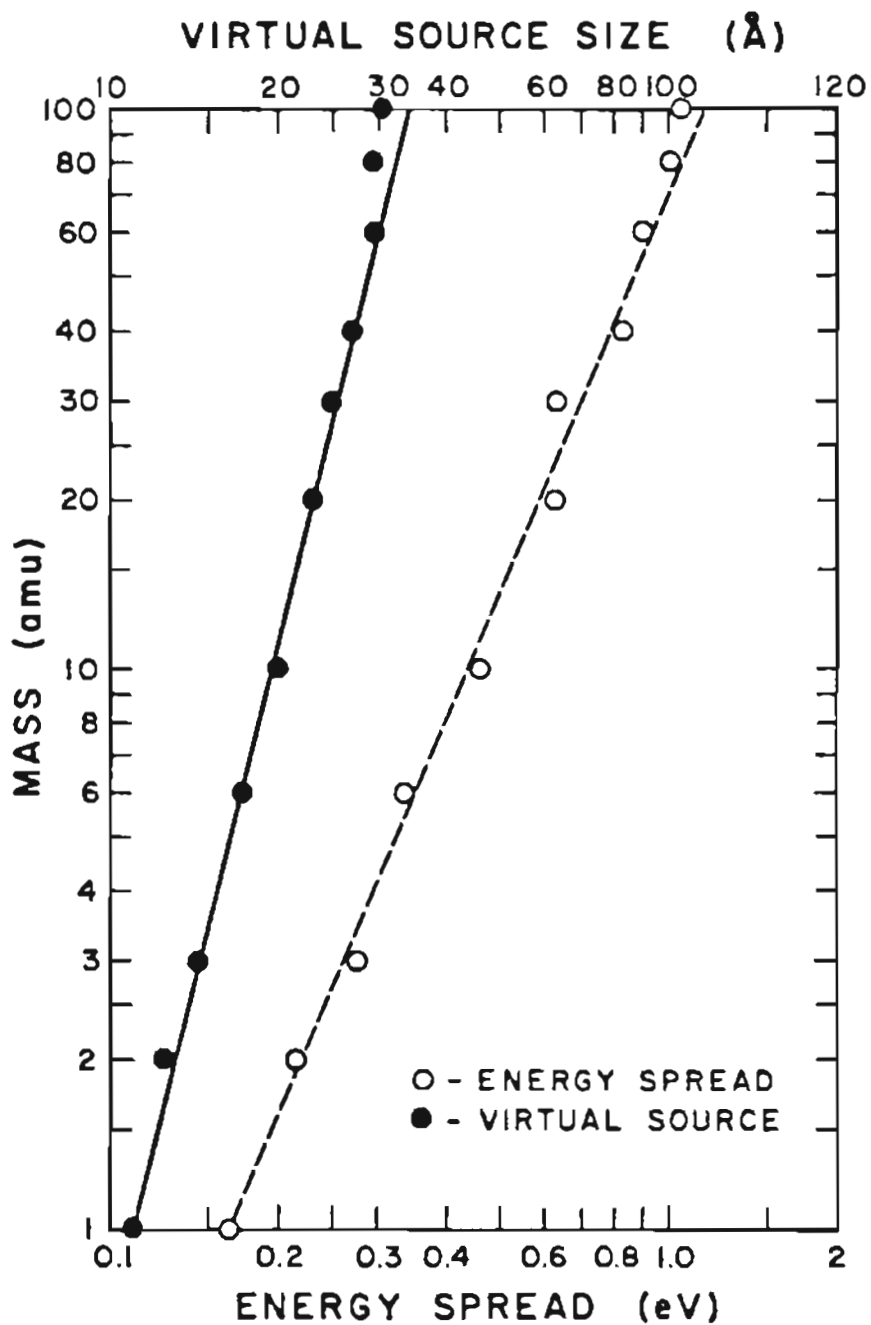Figure 12: Energy Spread and Virtual Source Size vs. Number of Particles (worst case, M = 100amu).

Figure 13: Energy Spread and Virtual Source Size vs. Mass (all parameters other than mass are the standard input parameters, see Table III).

the front and rear of the pack would experience asymmetric forces from the other particles. If this was the case, we would expect the first particles emitted to have the most energy and the last particles emitted to have the least energy. This is because the leading particle would be accelerated faster since all the other particles are behind it, and the trailing particle would not be accelerated as rapidly since all of the other particles are in front of it. If these end effects are substantial, then this effect should be seen. But we can see that this is in fact not the case from the figure 14 plot of the kinetic energy vs. emission order. If there were end effects, the energy verses emission order graph should have a negative slope to it (first particles with the most energy and last particles with least energy). We see in figure 14 that no such slope exists, so we conclude that the end effects are not substantial and that n = 120 is sufficient, even though we do not fill the entire electrode space.

Using a Cyber 170/760 (belonging to Tektronix at their Beaverton, Oregon site) with double precision (30 decimal places), 120 particles, 4,000 steps, and a flight distance of 0.1mm requires about 20 minutes of CPU time for each run.

3. Analysis of the Data

The two parameters of interest in this study were, the virtual source size and the energy spread. Let us first look at virtual source size, with respect to each of the experimental parameters.

3.1. Virtual Source Size

The virtual source size has already been described as that source seen by the first lens in an electron/ion optical system. We can see from figure 15 how the final
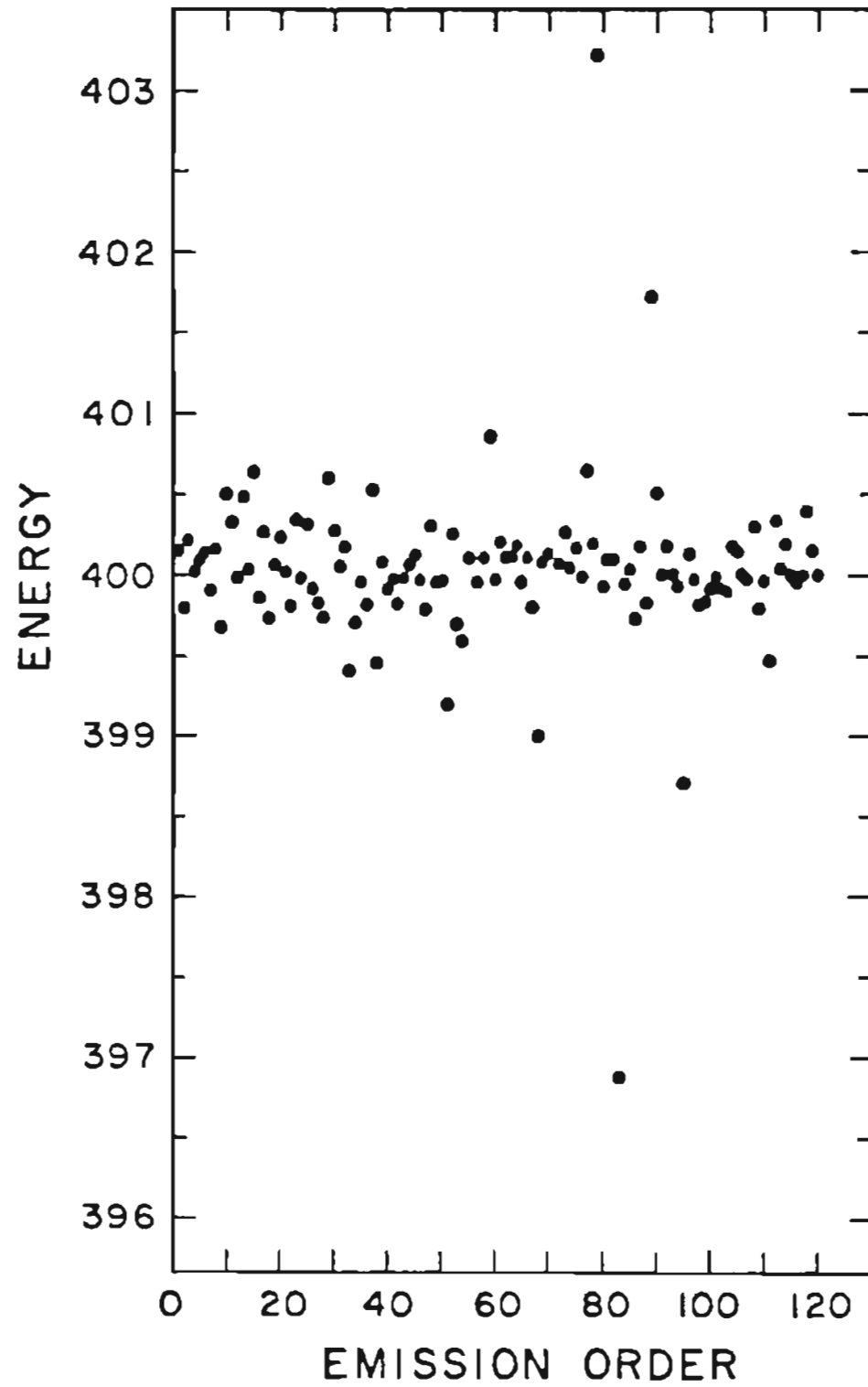
Figure 14: Final Energy vs. Emission Order using standard input parameters (see Table III).
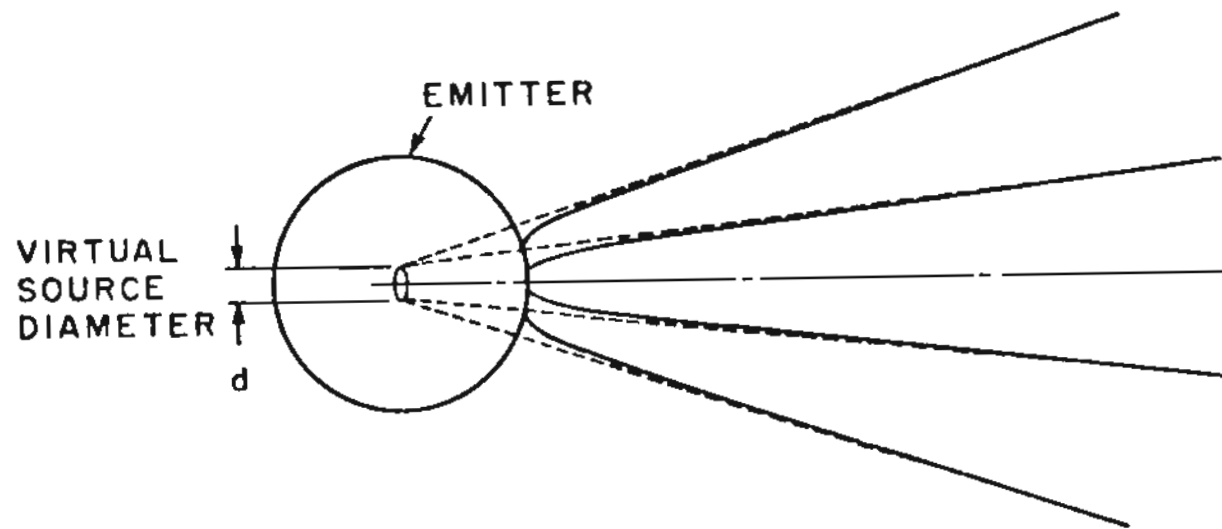
Figure 15: Diagram of how the virtual source size is obtained from trajectories.

direction of the trajectories is projected back from the reference plane to the virtual source plane. The virtual source is defined here as a circular ring containing 50% of the current. This is accomplished by finding the radius of the 60th particle (for the case of 120 total particles). The virtual source plane is now stepped along the z-axis and a new virtual source radius is found. If the new virtual source radius is smaller than the old radius, then the plane is again stepped in the same direction. If, on the other hand, the new virtual source radius is larger than the old radius, then we know we are traveling in the wrong direction and must reverse our direction. This is because we are trying to find the smallest possible radius of these backward projections. When it is decided that the direction of the steps must be reverse, the size of the steps are decreased by one order of magnitude. This process is continued with smaller and smaller steps until it is decided that the virtual source plane and virtual source size is determined to sufficient accuracy. This is how the virtual source size and position are determined.

In figure 16 we see that the virtual source size varies as the square root of the current. This is reasonable since as the current increases, interparticle distances decrease which cause the coulomb forces to be greater. The virtual source size increases as the 1/4 power of mass as seen in figure 13. A larger mass would mean a longer interaction time and therefore a greater radial broadening. An unexpected result shown in figure 17 is the lack of a charge dependence on the virtual source size. Figure 18 shows that there is an inverse square root dependence on the emitter radius, presumably because as the emitter radius increases, the area of emission increases and as a result, the interparticle distances increase causing the coulomb
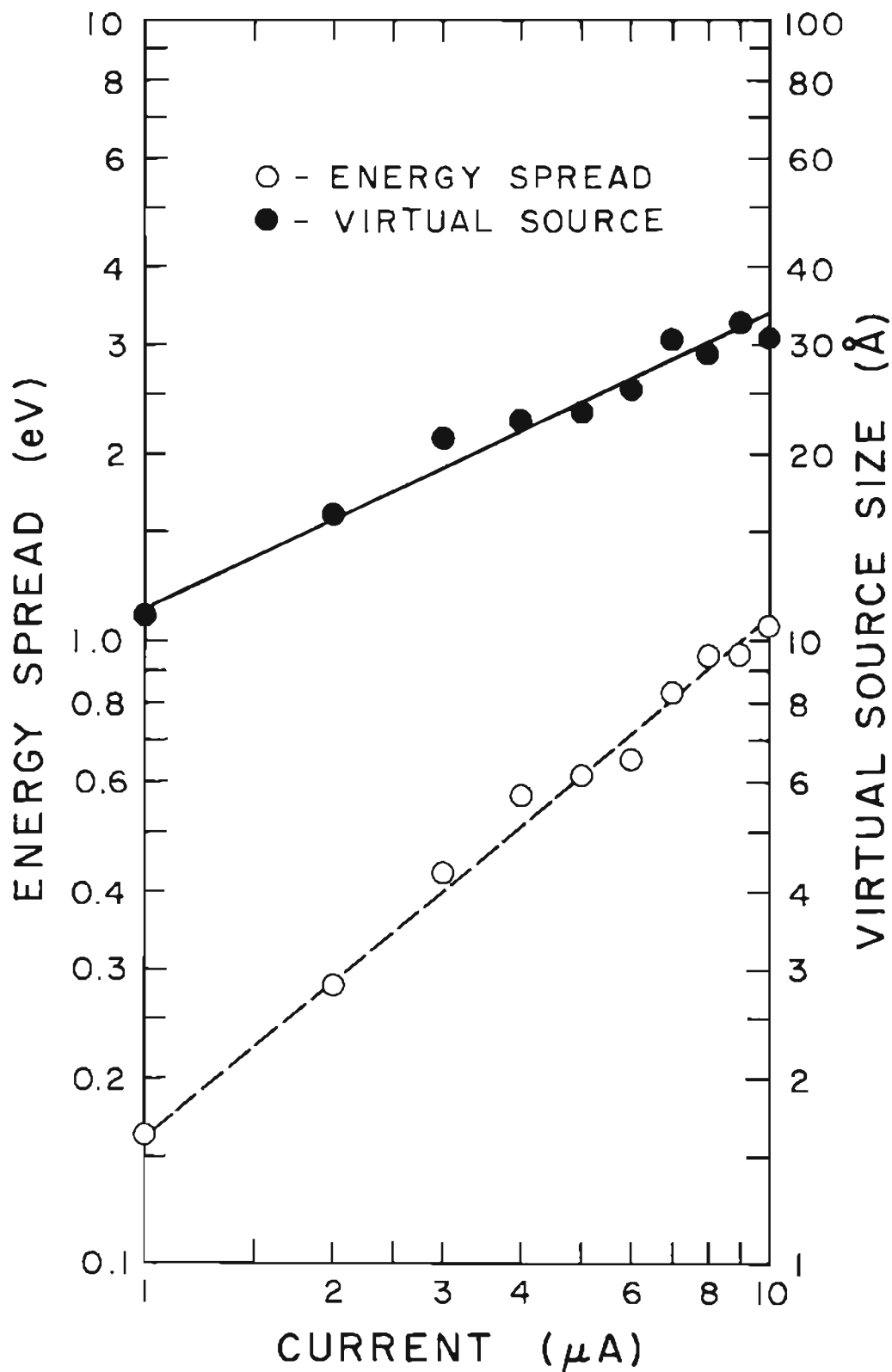
Figure 16: Energy Spread and Virtual Source Size vs. Current (all parameters other than current are standard, see Table III).
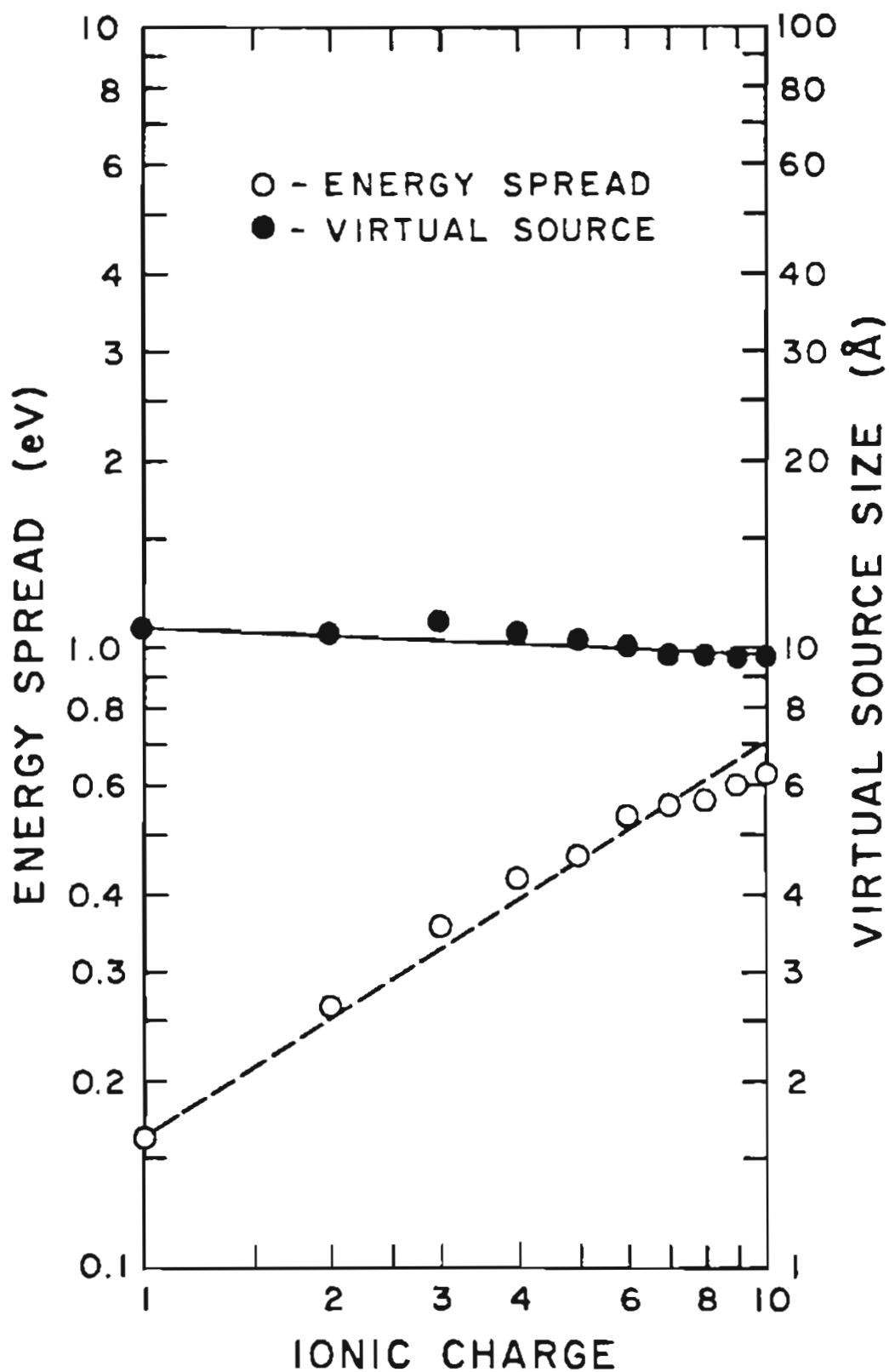
Figure 17: Energy Spread and Virtual Source Size vs. Ionic Charge (all parameters other than charge are standard, see Table III).
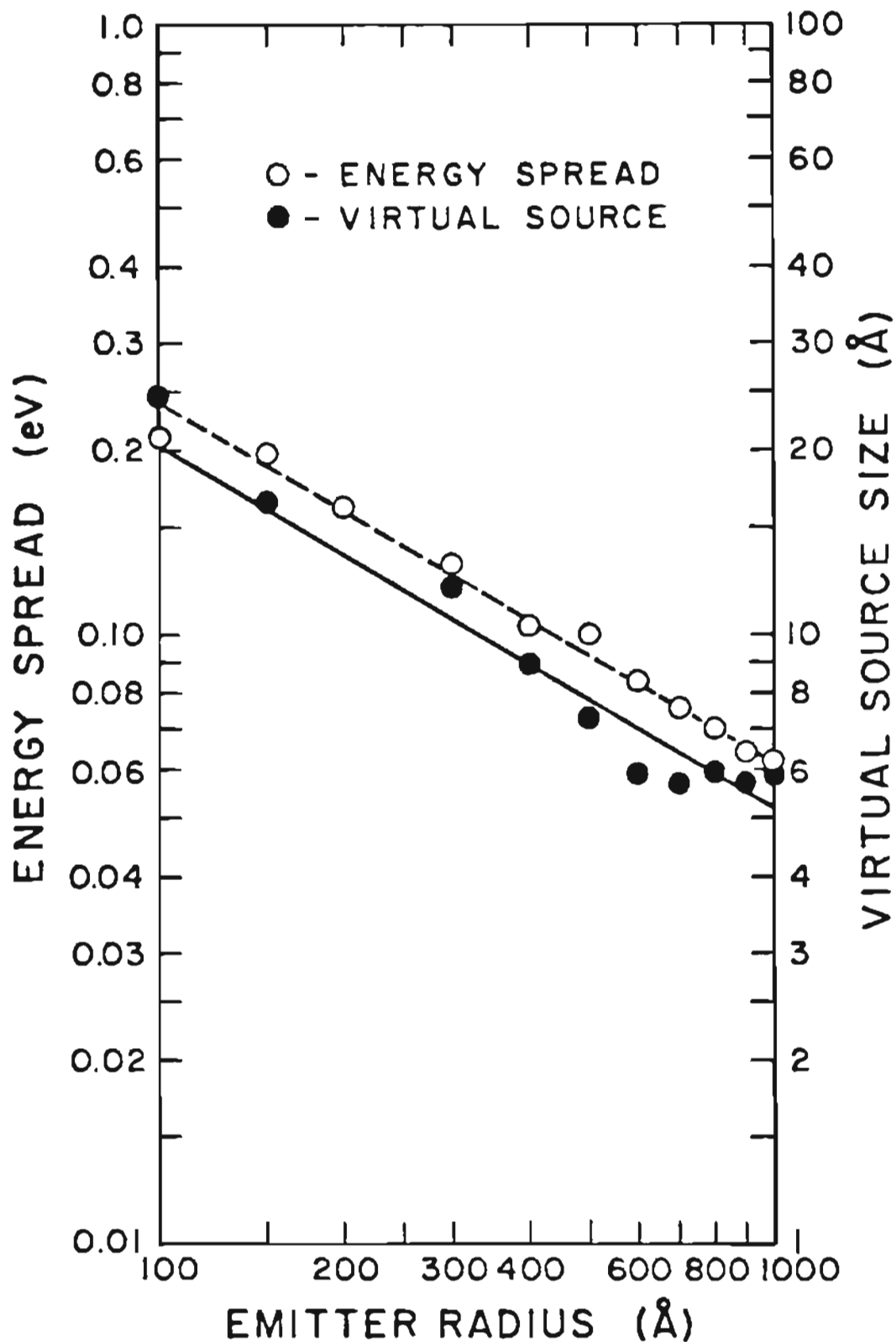
Figure 18: Energy Spread and Virtual Source Size vs. Emitter Radius (all parameters other than radius are standard, see Table III).

forces to be decreased. The virtual source size varies inversely with the electric field as seen in figure 19. This may be because a higher electric field increases the particle acceleration and thereby reduces the interaction time. Figure 20 shows that the virtual source size varies with the 1/4 power of the path length. As the flight path increases, the virtual source size is expected to increase because the particles have a longer period of time to interact. From figure 21 we see that the virtual source size is inversely proportional to the the beam half angle. This can be explained on the basis of the increases in interparticle distances with beam half angle. Figures 22 and 23 show no significant virtual source size dependence on either the initial kinetic energy or the initial kinetic energy spread. Next we will look at how the energy spread varies with these same experimental parameters.

3.2. Energy Spread

The energy spread was measured by taking the standard deviation of the values of the final particle energies after discarding the bottom and top 10% values.

This was another place where the original program was modified. Groves used a combination of curve fitting and some kind of non-standard full width at half maximum calculation to determine the energy spread. For reasons of ease of description as well as ease of calculation, the standard deviation from 10% to 90% of the final particle energies was used in this study. As before, there is no basis for using the 10 to 90% range in this calculation over the 20 to 80% range or the 25 to 75% range. Therefore, not the actual values of the energy spread, but rather the trends that these numbers give us are of primary interest.
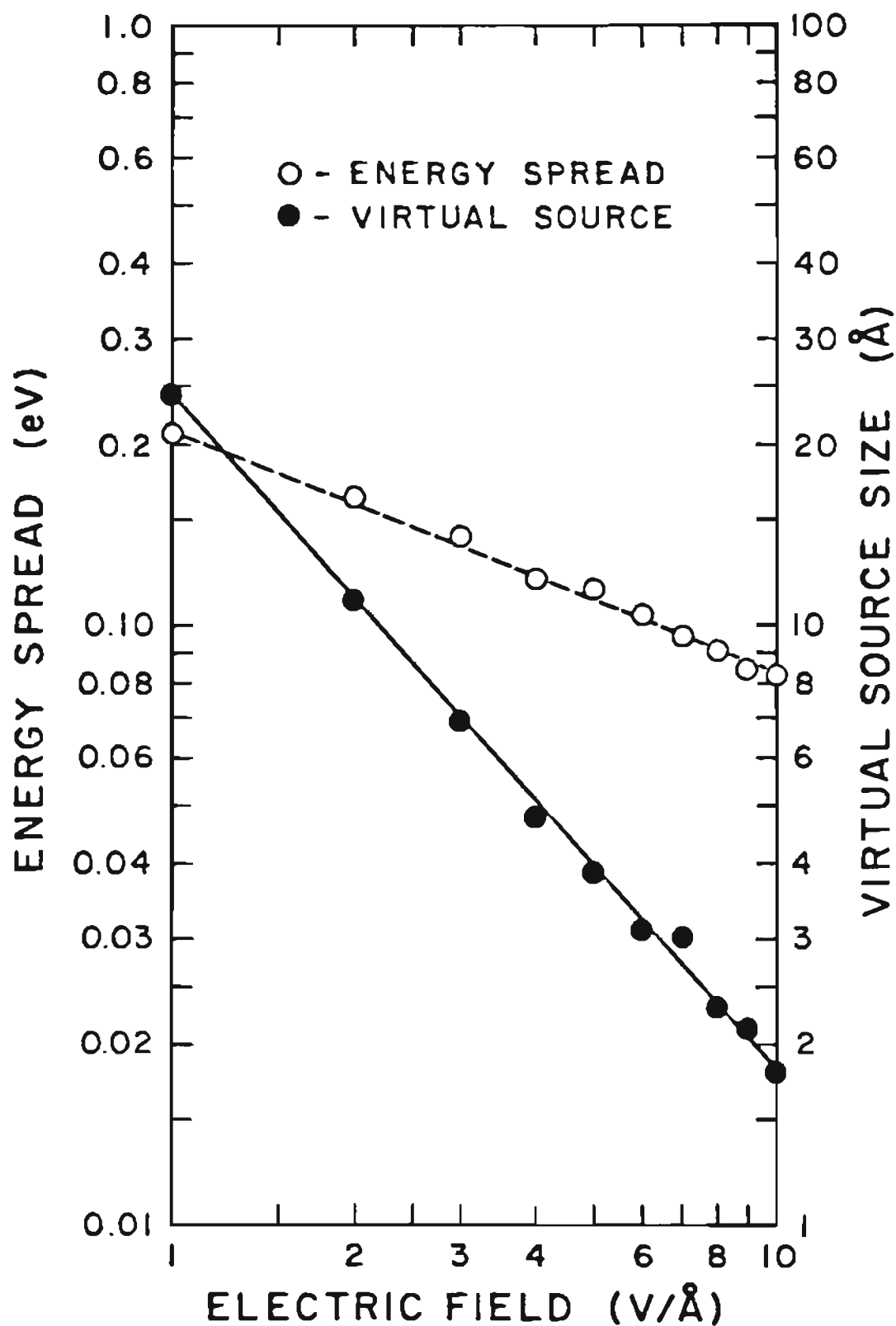
Figure 19: Energy Spread and Virtual Source Size vs. Electric Field (all parameters other than field are standard, see Table III).
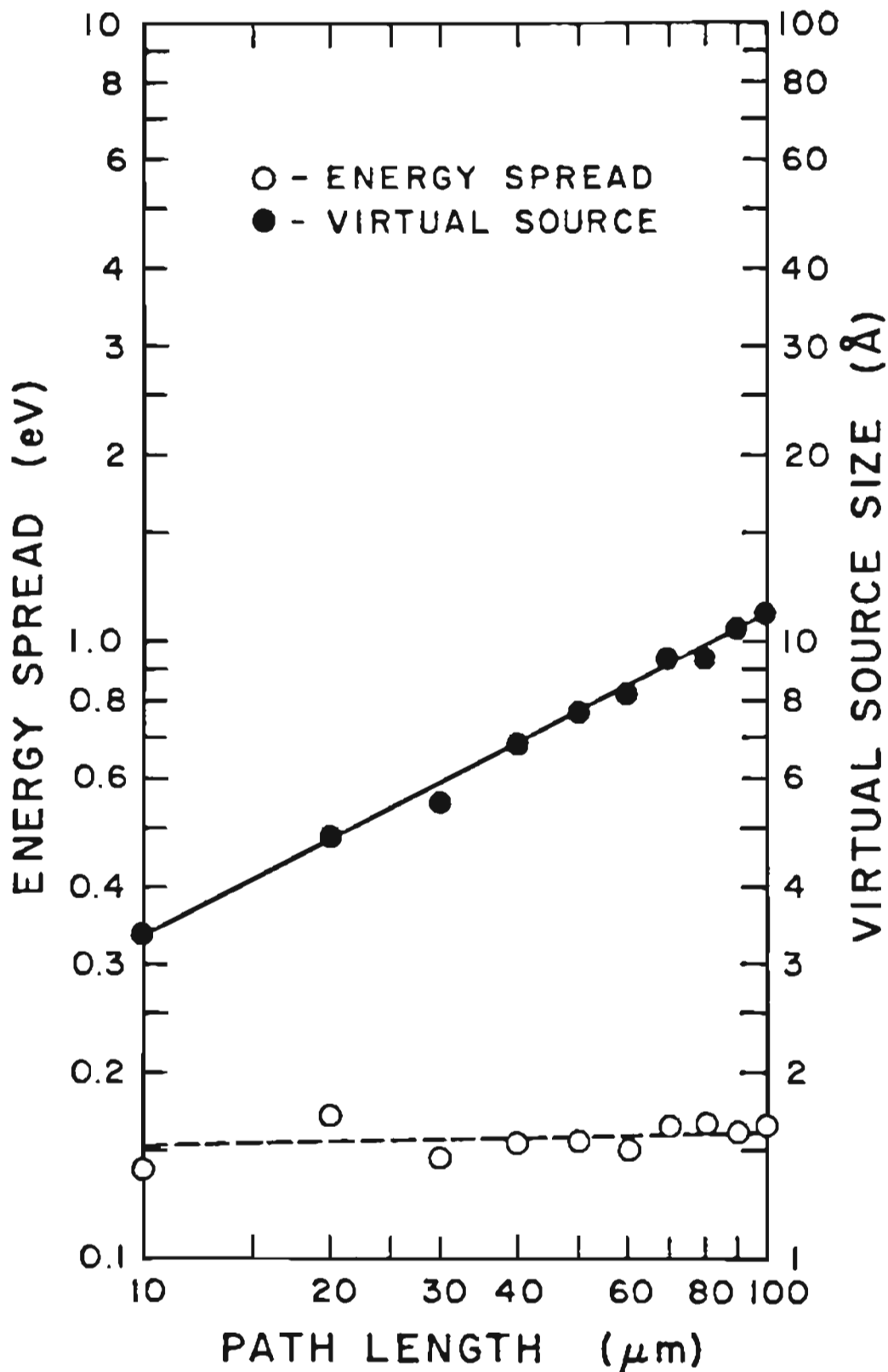
Figure 20: Energy Spread and Virtual Source Size vs. Path Length (all parameters other than path length are standard, see Table III).
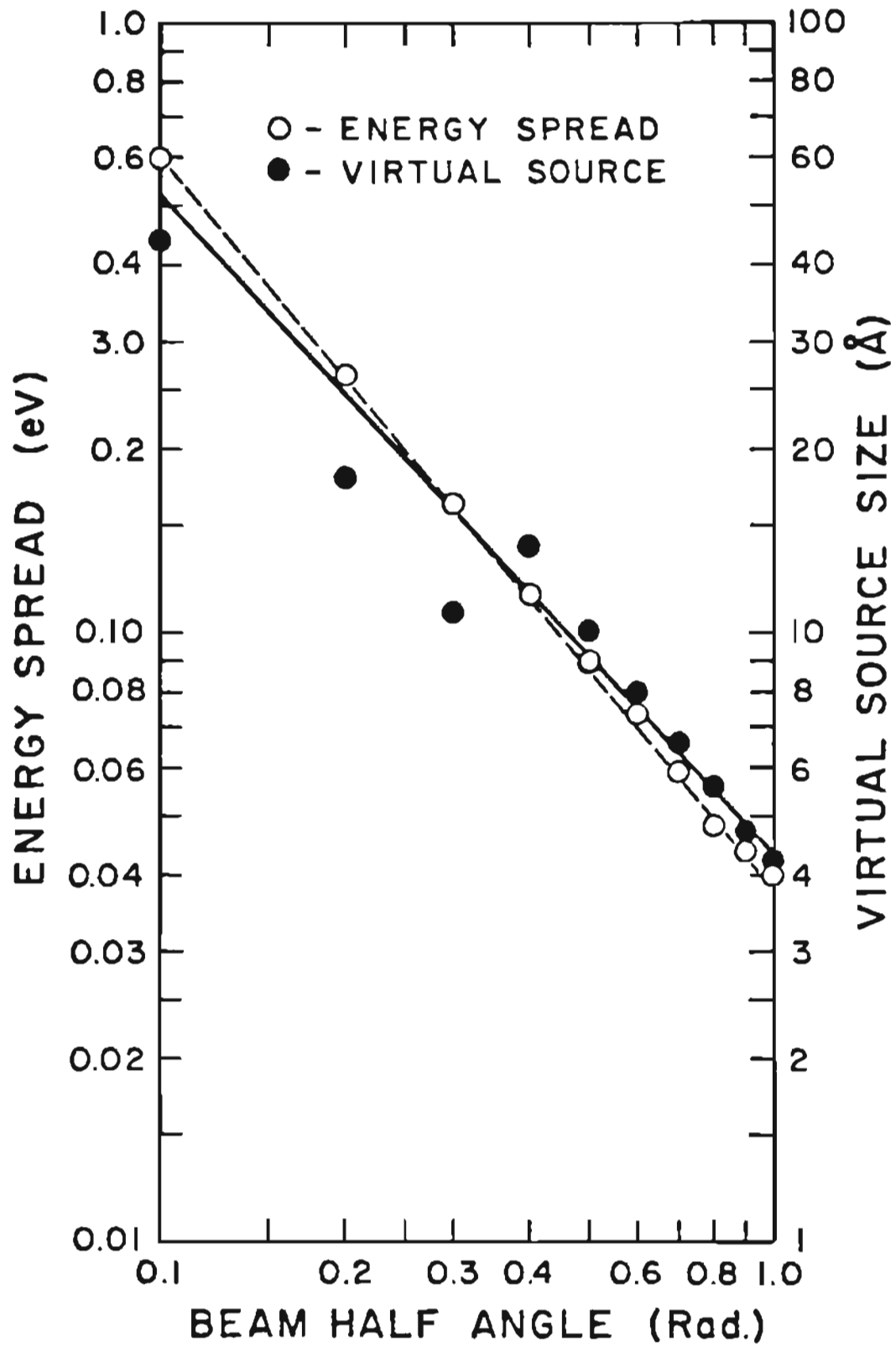
Figure 21: Energy Spread and Virtual Source Size vs. Beam Half Angle (all parameters other than beam angle are standard, see Table III).
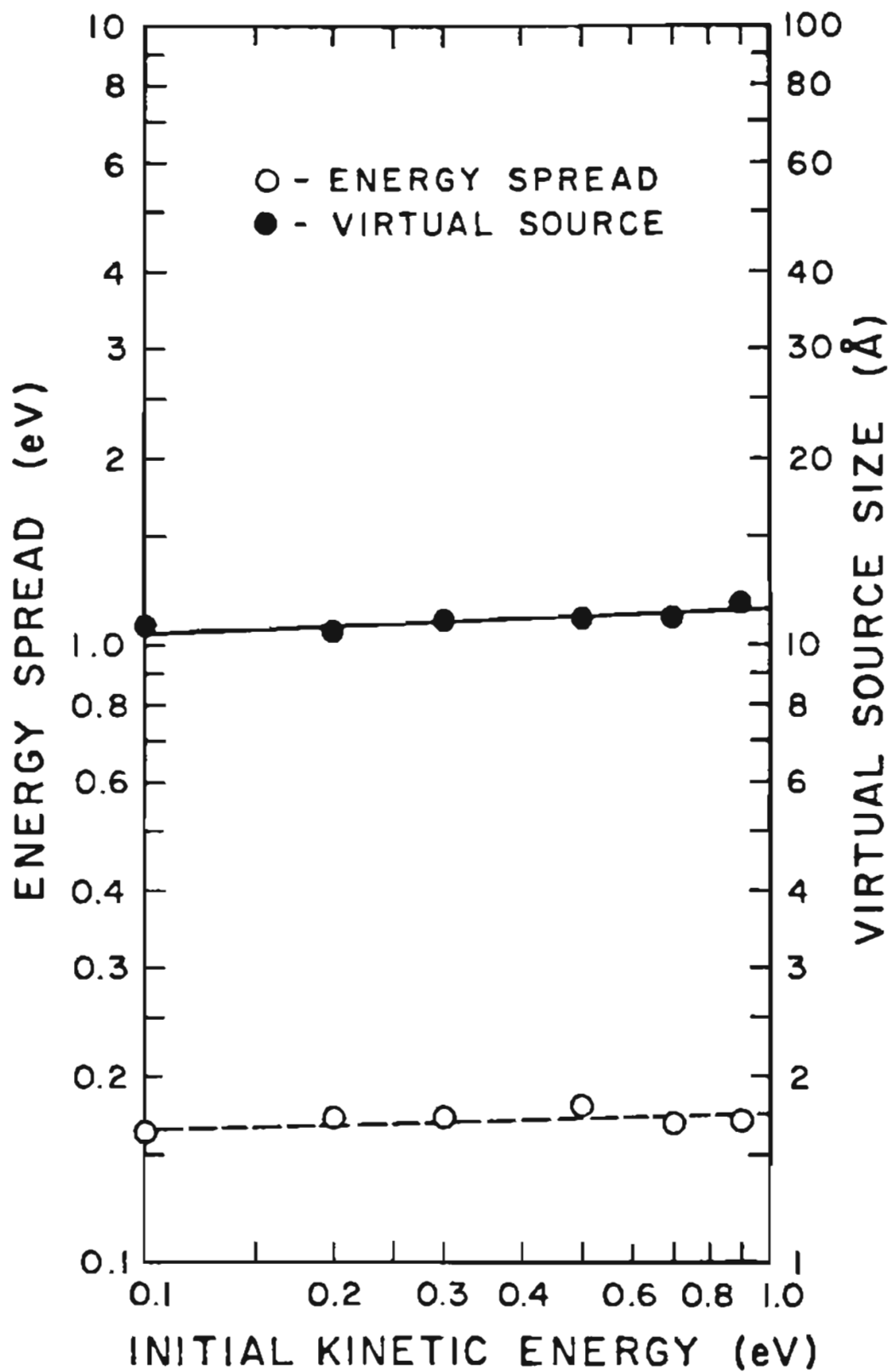
Figure 22: Energy Spread and Virtual Source Size vs. Initial Kinetic Energy (all parameters other than initial energy are standard, see Table III).
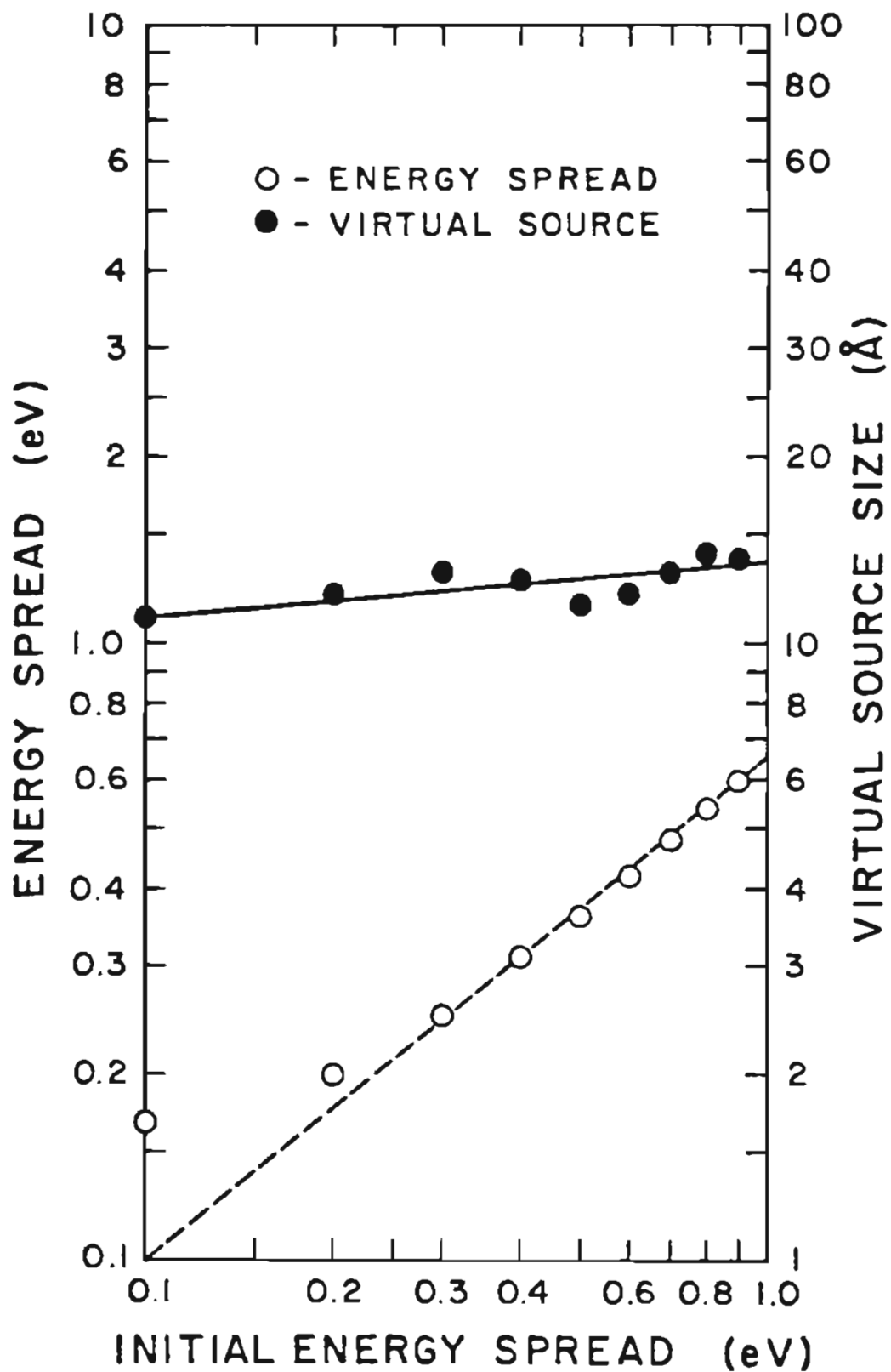
Figure 23: Energy Spread and Virtual Source Size vs. Initial Energy Spread (all parameters other than initial energy spread are standard, see Table III).

Looking at figure 16 again, we see that energy spread is proportional to the current. As current increases, interparticle distances decrease and energy transfer from one particle to another is facilitated. Energy spread increases with the square root of the mass as seen in figure 13. Again, as the mass increases, the interaction time increases and so does the spread of the energies. The energy spread increases as the square root of the ionic charge also. Another unexpected result is the increase in energy spread with charge. In figure 17, the energy spread is found to vary not inversely as is seen experimentally (figure 24 [45]), but proportionately with the square root of the charge. This difference may be due to the fact that we are using particles of charge 1 then 2 then 3 etc. exclusively, whereas in the experimental data, particles are a mixture of different charges.

The next experimental parameter of interest is the emitter radius. The energy spread varies inversely with the square root of the emitter radius [figure 18]. As the emitter radius increases, the interparticle distances decrease as does the energy spread. In figure 19 we see the energy spread varies inversely with the square root of the electric field. As the electric field increases, the interaction time decreases because the particles are traveling faster. The path length Z, on the other hand, has no effect on the energy spread as shown in figure 20 whereas the virtual source size increases with Z as discussed earlier. This is due to the fact that radial broadening is still occurring as the particles feel a general force away from the axis. Energy spread on the other hand is caused by forces along the z-axis, and their relaxation is complete within a short distance after they are emitted. Figure 21 is as we would expect, that is increasing beam angle increases the interparticle separa-
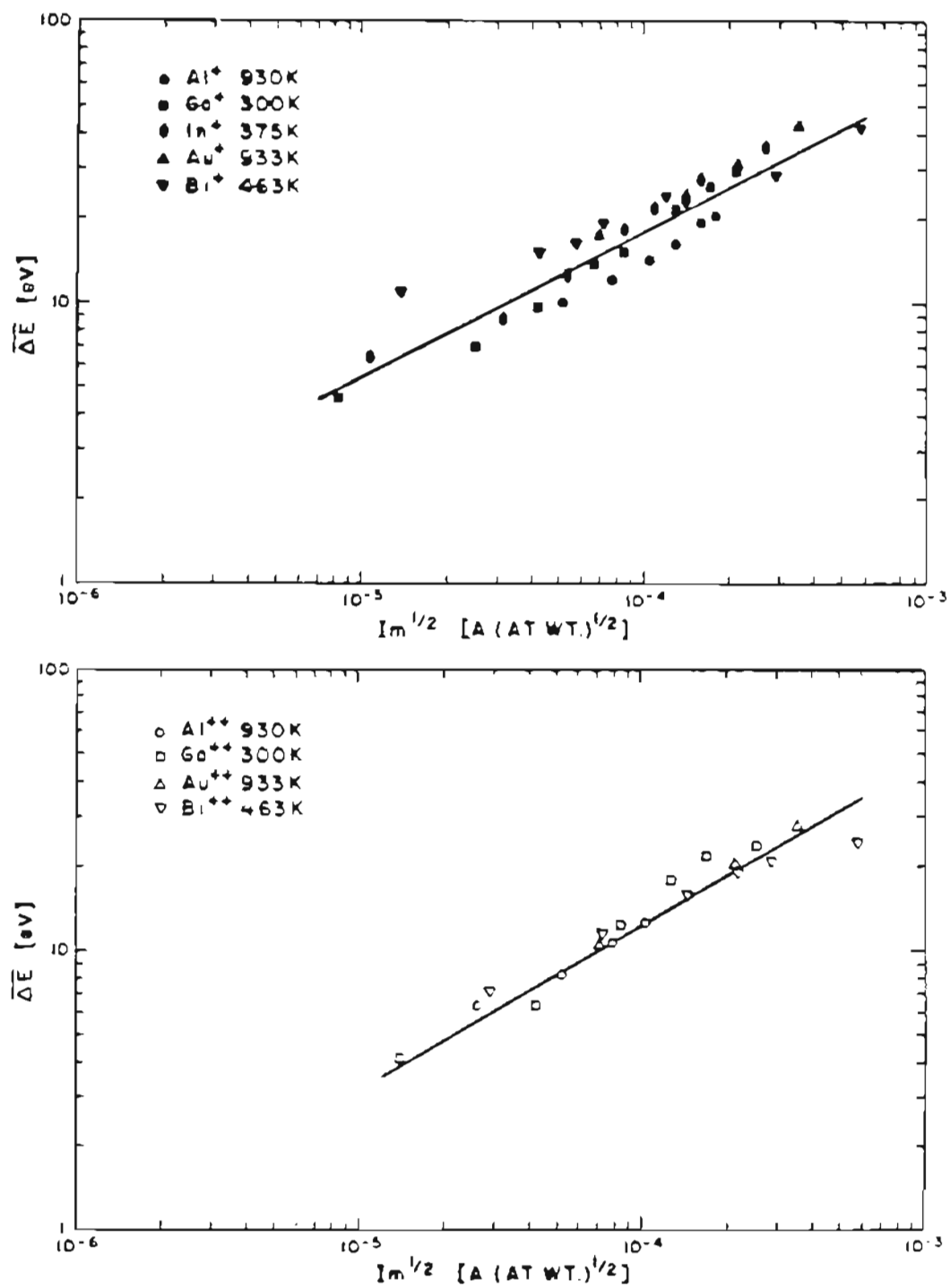
Figure 24: Experimental evidence for the $IM^{1/2}$ dependence on the energy spread.

tion and decreases the energy transfer of one particle to another. In figure 22 we observe that there is no energy spread dependence on the initial kinetic energy. Finally, in figure 23 we note that the final energy spread is proportional to the initial energy spread. Curiously, the final energy spread is less than the initial energy spread at high values of ΔE_i.

The empirical results can be summarized as follows:

$$\Delta E_c = .977 \; \frac{I}{\alpha} \left[\frac{Mq}{Fa} \right]^{1/2} eV \tag{32}$$

and

$$d = \frac{53.5}{F\alpha} \left[\frac{IM^{1/2}Z^{1/2}}{a} \right]^{1/2} \text{Å}. \tag{33}$$

Where $\Delta E_c \equiv$ energy spread (eV due to the coulomb interaction); $I \equiv$ current (μA); $M \equiv$ mass (amu); $q \equiv$ ionic charge ($1 = -1.602 \times 10^{-19}$coul); $\alpha \equiv$ beam half angle (rad); $F \equiv$ electric field (V/Å); $a \equiv$ emitter radius (Å); and $Z \equiv$ path length (μm).

4. Justification of the Model

The main reason to believe that this model is complete is that the predicted functional dependence is dimensionally consistent. The energy spread and virtual source diameter given in equations (32) and (33) were found to have dimensions of energy and length respectively. This shows that, among other things, no experimental parameters were left out. Another positive result is that $IM^{1/2}$ dependence that we obtained for the energy spread is also observed experimentally as shown in figure 24 for five different LMI sources.

For the case of $F = 3$ V/Å, $M = 70$mu, $a = 50$Å, $Z = 10^4 \mu$m, $\alpha = 0.3$ rad, $I = 5.6 \mu$A or $I' = 20 \mu$A/sr (where $I' \equiv$ angular intensity), the predicted values for virtual source size and energy spread from equation (32) and (33) are: $d = 357$Å and $\Delta E = 12.5$ eV. These results compare favorably with experimental results. For example Komuro, et al,[12] obtained experimentally a value of $d = 400 - 450$Å for low currents of a Ga LMI source; the value of ΔE at $I' = 20 \mu$A/sr is 5 to 10 eV [38].

Next we will consider the justification of the use of the spherical rather than the more realistic SOC emitter. In figure 2 the expected shape of the Taylor cone and the protrusion under operating conditions is given. If one used a spherical emitter to model the Taylor cone (lower circle in dotted lines), one could see that there would be rather substantial errors incurred. But looking at the protrusion in the same figure, we can see that modeling the end of the protrusion with a sphere (upper circle in dotted lines), is quite reasonable.

A study by J.W. Ward [31], where not only a SOC potential was used, but also the entire electrode space was filled with electrons (the two major differences between a real LMI source and this model) by limiting the total path length to 10^4 Å. In the latter study, only the virtual source size was determined, nevertheless the results compare very favorably with the results of this study. One can predict a 1/4 dependence on path length from his results also. This close agreement suggests that the use of a spherical emitter with an unfilled electrode space is valid.

Can we justify the use of error vectors transferred from a run without the mutual interaction of the particles to a run with the mutual interaction of the particles? This can be justified because only the predictions are modified. In the

Hamming predictor-corrector method, the closer the predictions are to the correct value, the fewer the iterations needed to converge on a predicted result, the less computer time is required. This is important because the bulk of the computation required is in the correction portion of Hamming's method.

And lastly, the number of particles and the number of steps used in the calculations were justified by having them increased to a point was reached where additional decreases in the step sizes and increases in the number of particles did not cause any significant change in the final results.

5. Other Interesting Results

An interesting result can be seen in figures 25 and 26. Figure 26 shows the initial, final and calculated distributions of the particles in time. It is clear that the initial distribution and the calculated Poisson distribution are virtually identical. It is also seen from this figure that the final distribution is not exactly the same as the initial distribution, showing that the distribution has been altered through the coulomb interactions after the particles were emitted. In figure 25, no such differentiation can be seen between the initial and final distributions. This is probably due to the lower current and less interactions between the particles. The calculated Poisson distribution in figure 25 is calculated for approximately 1.2 particles per time step, where in figure 26 it is done for .24 particles per time step. The initial distributions in both figures 25 and 26 are the same.

Another interesting and unexpected result of this study is depicted in figure 27, where it is seen that there are no particle trajectories that have both zero slope and
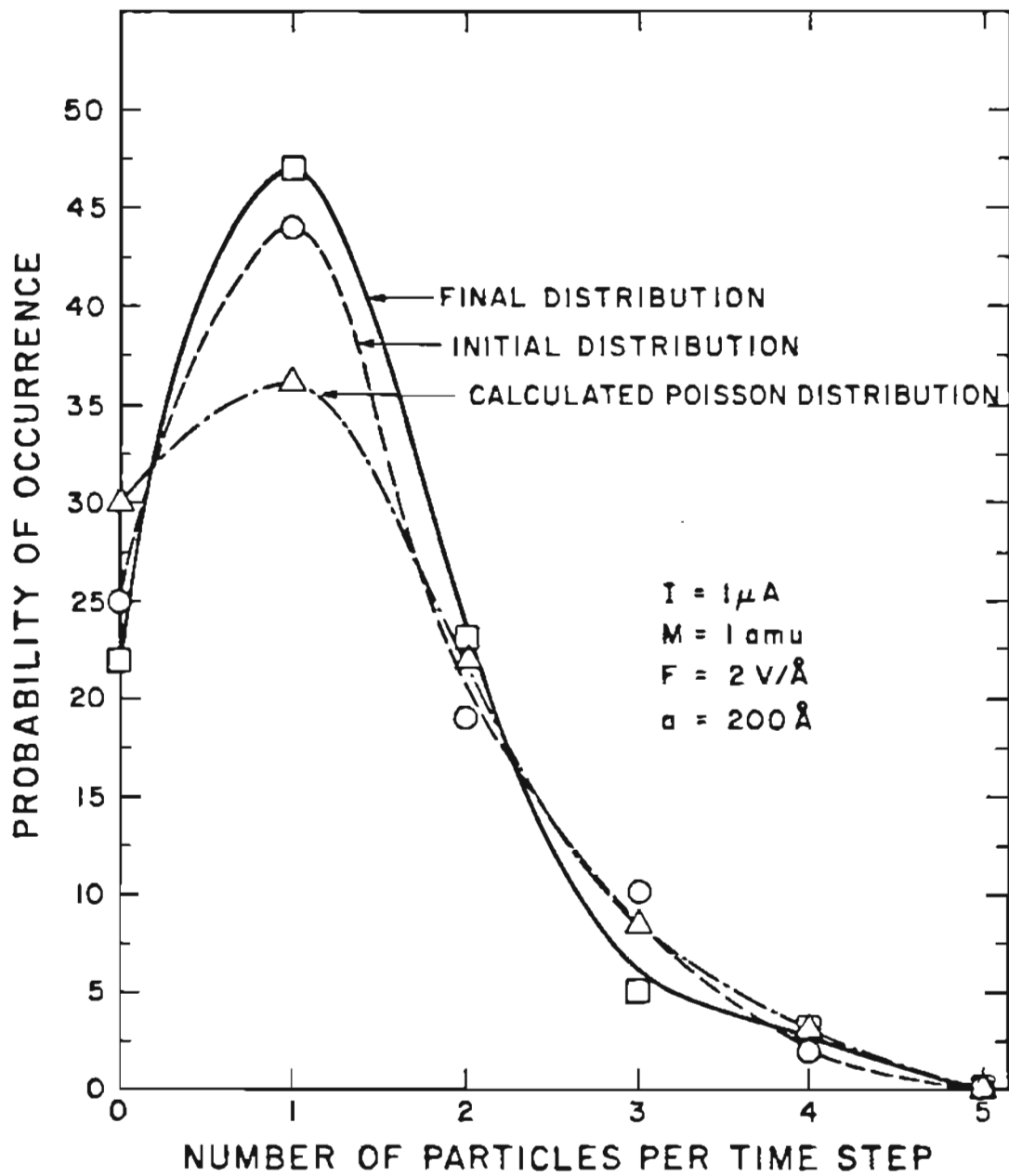
Figure 25: Time distribution of particles in the initial and final planes with all parameters at standard values (see Table III) compared with a Poisson distribution.
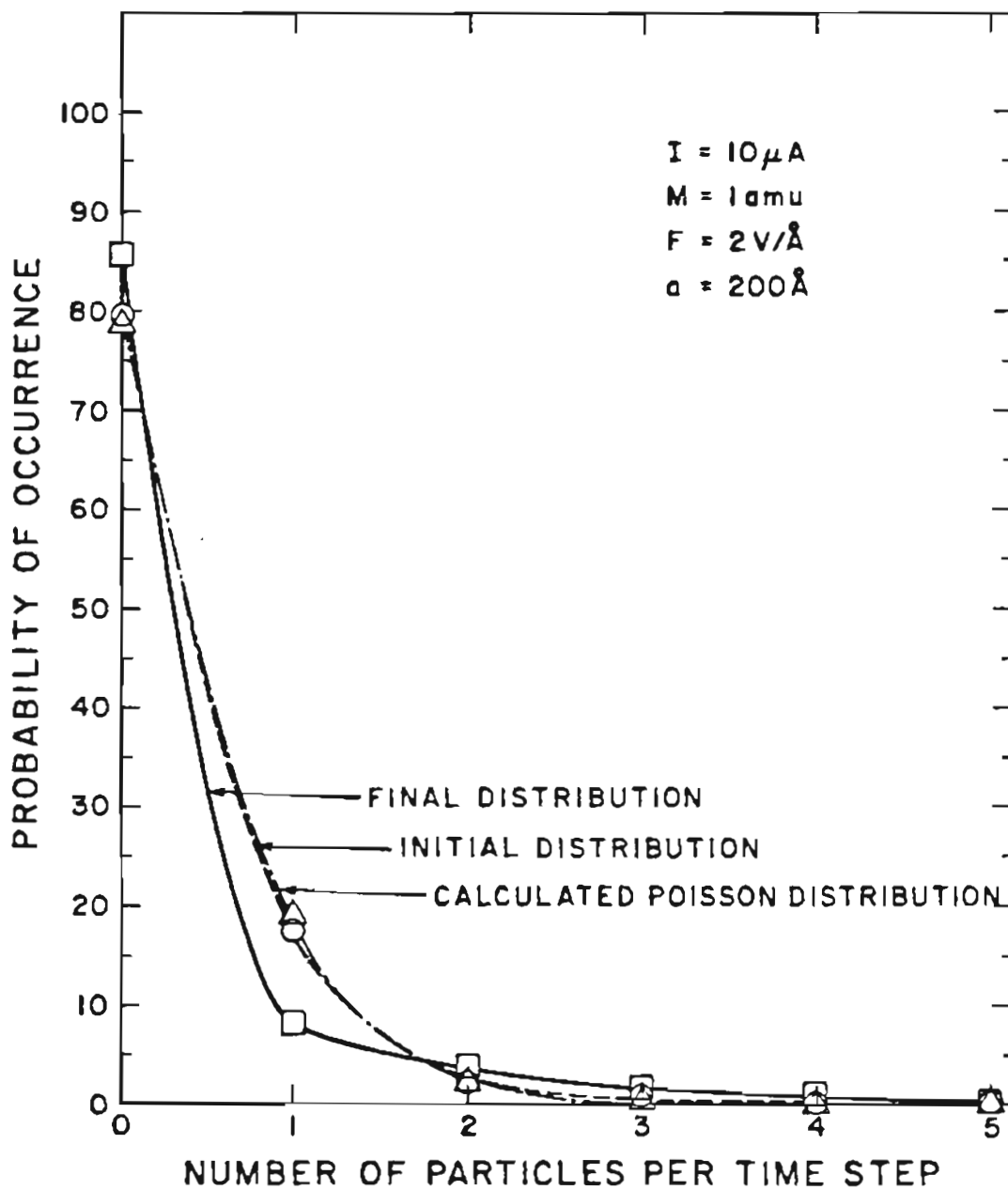
Figure 26: Time distribution of particles in the initial and final planes at 10μA with all other parameters at standard values (see Table III) compared with a Poisson distribution.
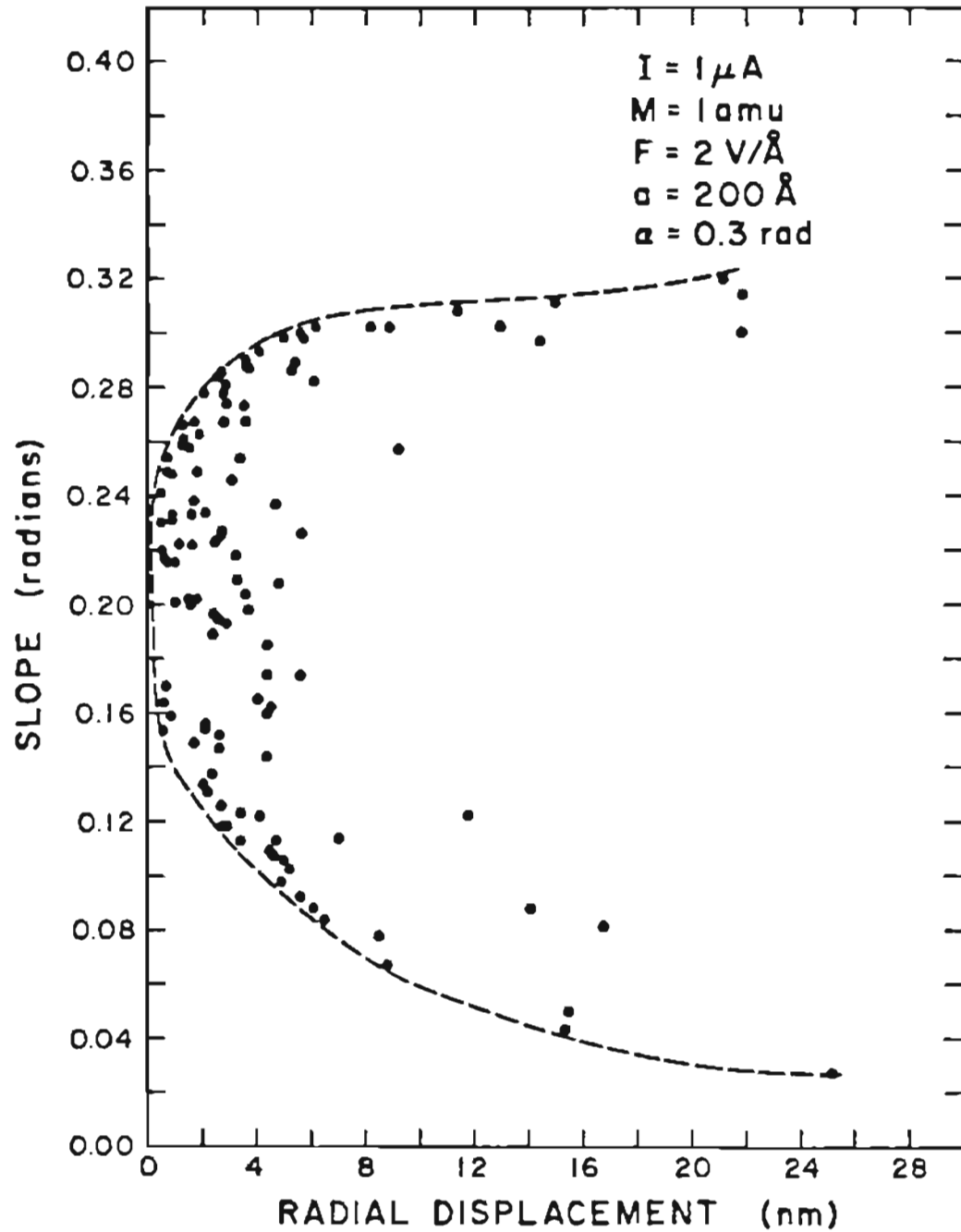
Figure 27: Trajectory Slope vs. Radial Displacement in the virtual source plane with all parameters at standard values (see Table III).

zero radial displacement in the virtual source plane. In order to have some particle trajectories near the axis we must have either (1), particle trajectories whose backward projections lie along the axis, or (2), particle trajectories which end up on the axis at the final reference plane but project backwards with a negative slope to be off the axis in the virtual source plane. We do not have any particles of the first variety projecting along the axis because we have no particles which have both zero slope and zero displacement (points at the origin). And we do not have any particles of the second variety because we have no particles with a negative slope.

The results for current density vs. radial displacement are depicted in figure 28 in the virtual source plane and angular intensity vs. trajectory angle in the final plane is plotted in figure 29 at a mass of 1 amu for three separate currents and the same thing is plotted in figure 30 for a constant current of 1μA for two separate masses. In both cases, all other parameters are at their standard values (see Table III). Figure 28 shows that the current density distribution in the virtual source plane is not Gaussian as is commonly assumed. Figure 29 show the dip in angular intensity on axis in qualitative agreement with experimental results [46]. However, the increase in beam angular divergence with current and mass is not seen. This supports earlier conclusions that the reason for this divergence is primarily due to an increase in emitting area [47,48].

6. Conclusions

We have found that the energy spread varies directly with the current, and the square root of the mass and charge. It also varies indirectly with the emission angle and the square root of both the field and the emitter radius. The virtual source size
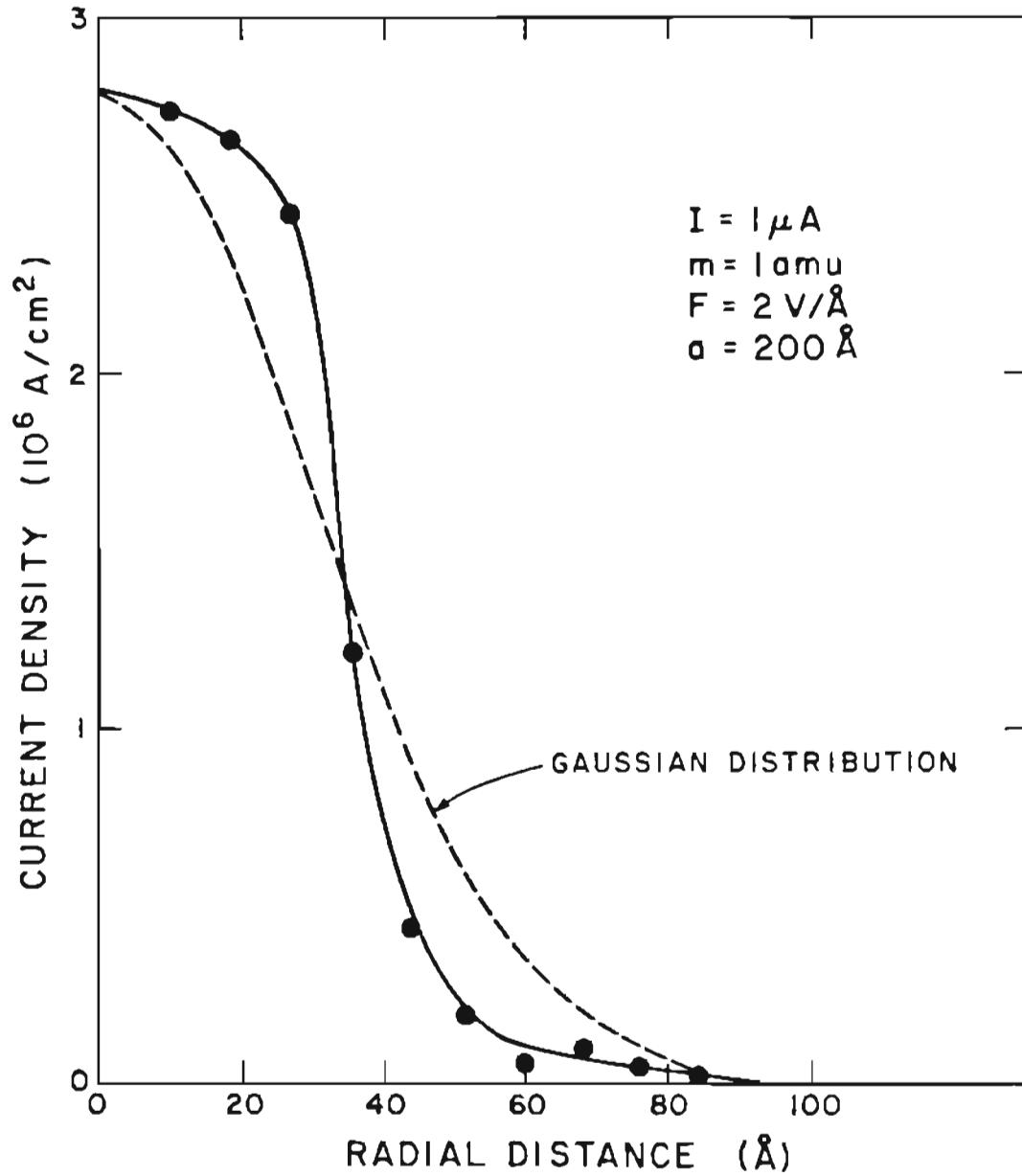
Figure 28: Current Density vs. Radial Displacement in the virtual source plane with all parameters at standard values (see Table III).
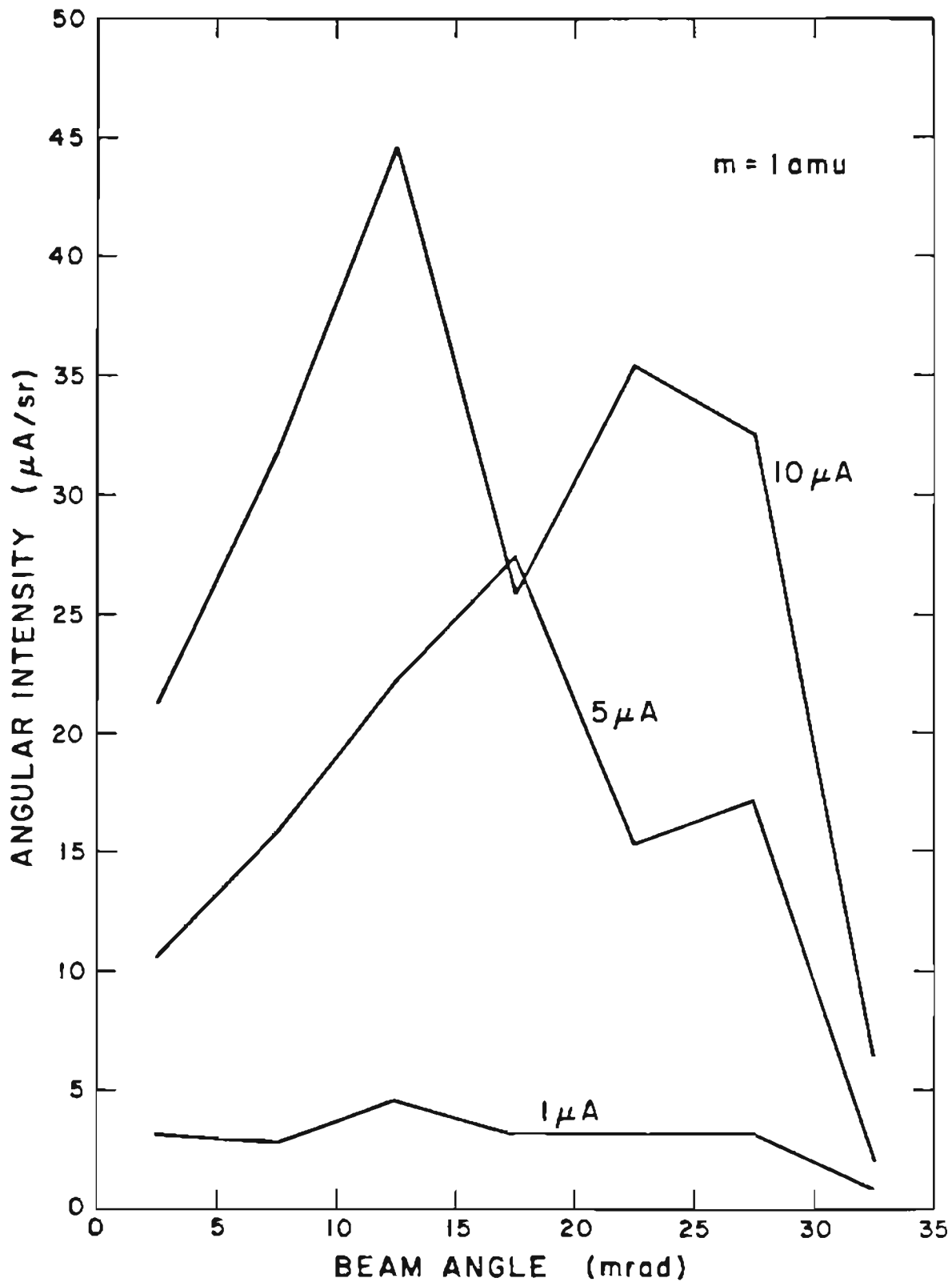
Figure 29: Angular Intensity vs. Beam Angle in the reference plane at 1, 5 and $10\mu A$ with all other parameters at standard values (see Table III).
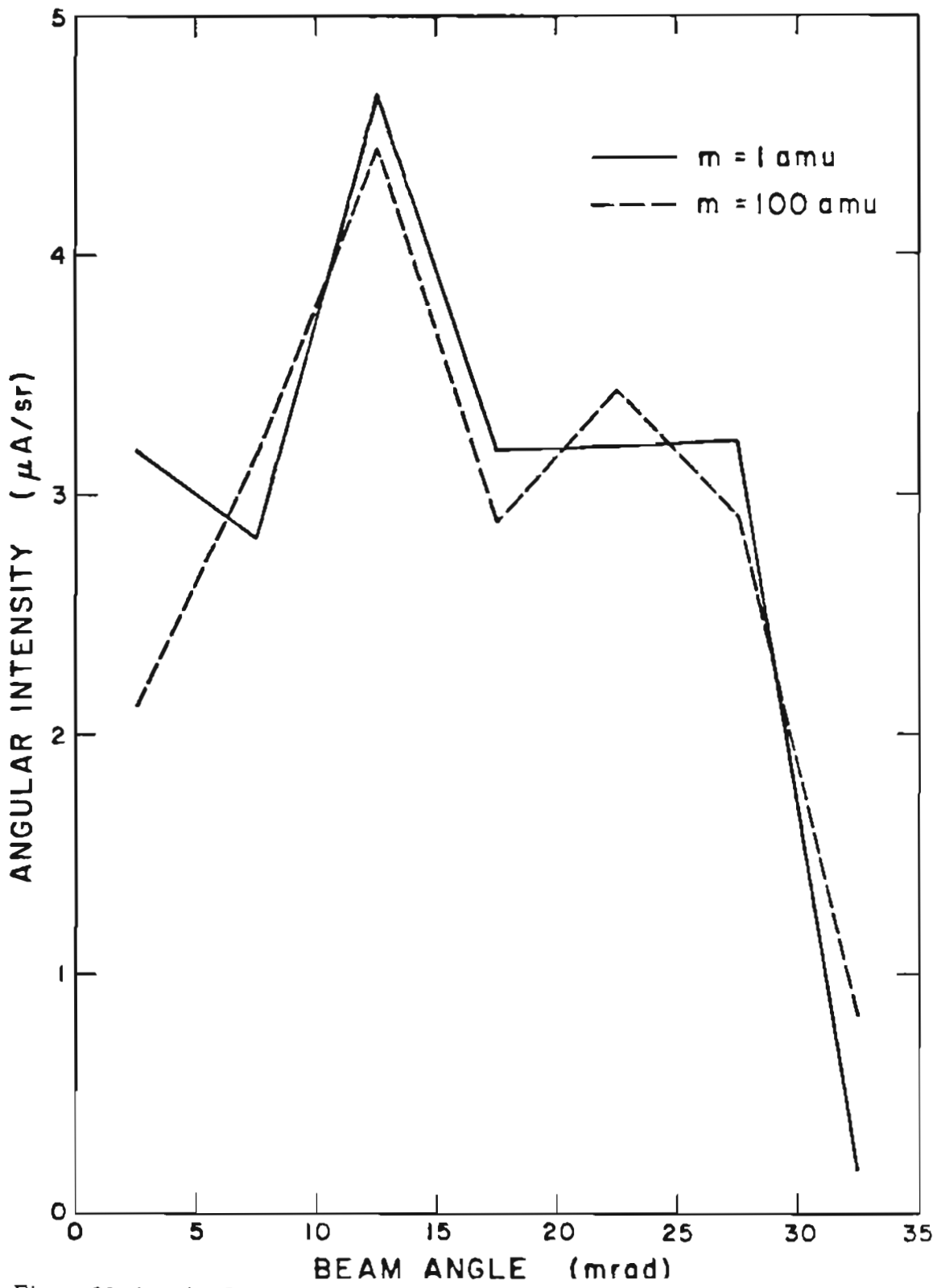
Figure 30: Angular Intensity vs. Beam Angle in the reference plane at 1 and 100amu with all other parameters at standard values (see Table III).

was found to vary directly with the square root of the current and with mass and total flight distance to the one fourth power. It was also found to vary indirectly with the field, the emission angle, and the square root of the emitter radius.

We have found the trends of all of the important experimental parameters and have shown by means of the functional dependence that no other parameters are necessary, therefore we have a complete set of all of the experimental parameters. If the experimental value of the virtual source size and energy spread are known for one specific example of the parameters, a simple adjustment in the empirical results can, I believe, predict the virtual source size and energy spread due to the coulomb interactions.

Appendix A

Using a Random Number Generator to Compute
a Random Variable of Known Distribution.

It is sometimes important in numerical simulations to be able to generate a random variable which follows a certain prescribed distribution. A common example of a distribution is the Gaussian or "bell shaped" distribution which is distributed about some mean value. While the wanted distribution may be Gaussian or any other arbitrary distribution, the distribution given by the random number generator is usually a uniform distribution between zero and one. In a uniform distribution, there is an equal likelyhood that the number generated will fall anywhere within the interval between zero and one and no possibility that it will fall outside of that interval. One would like to be able to mold that uniform distribution into any wanted distribution.

A statement of the problem is as follows:

Given a random number X, uniformly distributed between zero and one, we wish to generate a number Y, distributed according to the known distribution $N(Y)$.

The solution is derived from the supposition that Y is derived from X by a one-to-one mapping. The distribution of X can be called $M(X)$, and can be given by

$$M(X) = \begin{cases} 1 & 0 \leq X \leq 1 \\ 0 & \text{otherwise} \end{cases}$$

Assuming $Y(X)$ exists, we can integrate M and N over similar intervals, and the

area should be the same. That is,

$$\int_X^0 M(X)\, dX = \int_{Y(X)}^{Y(0)} N(Y)\, dY$$

Since we know N(Y), the integral can be found (at least in principle). N(Y) must be

normalized so that

$$\int_1^0 N(Y)\, dY = 1$$

Let us define a function f(Y) by

$$f(Y) = \int_Y^{Y(0)} N(Y)\, dY$$

Assuming that f(Y) is known, and where $Y_0 = Y(0)$. We must assume a value for

Y_0, and this amounts to arbitrarily specifying Y(X) at one point (X = 0). Since

$$\int_X^0 M\, dX = X$$

we have the result

$$Y = f^{-1}(X)$$

where f^{-1} is the inverse function of f. This completes the proof of the theorem given

in the text.

References

[1]   N. Anazawa, R. Aihara, M. Okunuki and R. Shimizu, Scanning Electron Microscopy IV (1982) 1443.

[2]   A.R. Waugh, A.R. Bayly and K. Anderson, Proc. 29th Int. Field Emission Symp. (Göteborg, Sweden, 1982).

[3]   R.L. Seliger, R.L. Kubena, R. Olney, J.W. Ward, and V. Wang, J. Vac. Sci. Tech. 16 (1979) 161.

[4]   M. Komuro, H. Hiroshima, H. Tanoue, and T. Kanayama, J. Vac. Sci. Tech. B 1 (1983) 985.

[5]   L.W. Swanson and L.C. Crouser, Phys. Rev. 163 (1967) 622.

[6]   A.E. Bell and L.W. Swanson, Phys. Rev. B 19 (1979) 3353.

[7]   R. Speidel, D. Kurz, and K.H. Gaukler, Optik 54 (1979) 257.

[8]   G.I. Taylor, Proc. R Soc (London) 280A (1964) 383.

[9]   D.R. Kingham and L.W. Swanson, Vacuum 34 (1984) 491.

[10] P. Sudraud, 30th Int. Field Emission Symp., Philadelphia, PA (1983).

[11] E. Miyauchi, H. Arimoto, H. Hashimoto, and T. Utsumi, J. Vac. Sci. Tech. B 1 (1983) 1113.

[12] M. Komuro, T. Kanayama, H. Hiroshima, and H. Tanoue, Appl. Phys. Letrs. 42 (1983) 908.

[13] R. Speidel and D. Kurz, Optik $\underline{49}$ (1977) 173.

[14] O.W. Richardson and C.F. Brown, Phil. Mag. $\underline{16}$ (1908) 353.

[15] W. Schottkey, Ann. Phys. $\underline{44}$ (1914) 1101.

[16] H. Boersch, Z Physics. $\underline{139}$ (1954) 115.

[17] K.H. Loeffler, Z. Angew. Phys. $\underline{27}$ (1969) 145.

[18] B. Zimmermann, Adv. Electronics and Elec. Phys. $\underline{29}$ (1970) 257.

[19] T. Sasaki, Proceedings of VLSI Conf. (Pasadena, 1979), p. 125.

[20] A.B. El-Kareh and M.A. Smithers, J. Appl. Phys. $\underline{50}$ (1981) 455.

[21] H.C. Pfeiffer, 11th Symp. on Electron, Ion, and Laser Beam Tech. (San Francisco, 1971), p. 239.

[22] E. Goto, T Soma, M. Idesawa and T. Sasaki, 8th Int. Conf. on Electron and Ion Beam Sci. Tech. (Seattle, 1978), p. 135.

[23] A.V. Crew, Optik $\underline{50}$ (1978) 205.

[24] A.V. Crew, Optik $\underline{52}$ (1978/79) 337.

[25] T.R. Groves, D.L. Hammond, and H.P. Kuo, J. Vac. Sci. Tech. $\underline{16}$ (1979) 1680.

[26] J.W. Ward and R.L. Seliger, J. Vac. Sci. Tech. $\underline{19}$ (1981) 1082.

[27] W. Knauer, J. Vac. Sci. Tech. $\underline{16}$ (1979) 1676.

[28] H. Rose and R. Spehr, Optik $\underline{57}$ (1980) 339.

[29] W. Kanuer, Optik $\underline{59}$ (1981) 335.

[30] T. Sasaki, J. Vac. Sci. Tech. $\underline{21}$ (1982) 695.

[31] J.W. Ward, J. Vac. Sci. Tech. $\underline{3}$ (1985) 207.

[32] G.H. Jansen, T.R. Groves and W. Steickel, J. Vac. Sci. Tech. $\underline{3}$ (1985) 190.

[33] P.S. Dayan and G.A.C. Jones, J. Vac. Sci. Tech. 19 (1981) 1094.

[34] V.R.M. Rao, G.A.C. Jones, and H. Ahmed, J. Vac. Sci. Tech. 19 (1981) 1098.

[35] T.R. Groves, J. Vac. Sci. Tech. 19 (1981) 1106.

[36] A.E. Bell, G.A. Schwind, and L.W. Swanson, J. Appl. Phys. 53 (1982) 4602.

[37] L.W. Swanson, G.A. Schwind, A.E. Bell, and J.E. Brady, J. Vac. Sci. Tech. 16 (1979) 186.

[38] L.W. Swanson, G.A. Schwind, and A.E. Bell, J. Appl. Phys. 51 (1980) 3453.

[39] Y.W. Yau, T.R. Groves, and R.F.W. Pease, J. Vac. Sci. Tech. B 1 (1983) 1141.

[40] T.R. Groves, private communication.

[41] J.C. Wiesner, Point Cathode Electron Sources, Part III p.18

[42] A. Cromer, Am. J. Phys. 49 (1981) 455.

[43] A. Ralston, Mathematical Methods for Digital Computers, Wiley (1974).

[44] P.R. Bevington, Data Reduction and Error Analysis for the Physical Sciences, McGraw-Hill (1976).

[45] M.A. Gesley, Journal De Physique 45 (1984) 167.

[46] N.K. Kang, D. Tuggle and L.W. Swanson, Proc. 29th Int. Field Emission Symp. (Götenborg, Sweden, 1982), p.101

[47] N.K. Kang and L.W. Swanson, Appl. Physics A. 30 (1983) 95.

[48] A.J. Dixon, A. von Engle, Inst. Phys. conf. Ser. No. 54 (1980) 292.

Figures

[1] Schematic of Taylor cone on needle shaped substrate.

[2] Schematic of Taylor cone with protrusion.

[3] Diagram of the virtual source formation.

[4] Sphere-on-Orthogonal-Cone and it's potential.

[5] Schematic of spherical emitter with cone of emission defined.

[6] Schematic of an emission from a sphere and the virtual source formation due
     to the non-zero transverse velocity.

[7] Diagram showing the initial emission position and direction.

[8] Schematic of spatial bunching of emission (a) and removal of bunching (b).

[9] Energy Spread and Virtual Source Size vs. Number of Steps.

[10] Packet of particles traveling between electrodes.

[11] Energy Spread and Virtual Source Size vs. Number of Particles (standard
     input parameters, see Table III).

[12] Energy Spread and Virtual Source Size vs. Number of Particles (worst case).

[13] Energy Spread and Virtual Source Size vs. Mass (all parameters other than
     mass are standard input parameters, see Table III).

[14] Final Energy vs. Emission Order using standard input parameters (see Table
     III).

[15] Diagram of how the virtual source size is obtained from trajectories.

[16] Energy Spread and Virtual Source Size vs. Current (all parameters other than current are standard, see Table III).

[17] Energy Spread and Virtual Source Size vs. Ionic Charge (all parameters other than charge are standard, see Table III).

[18] Energy Spread and Virtual Source Size vs. Emitter Radius (all parameters other than emitter radius are standard, see Table III).

[19] Energy Spread and Virtual Source Size vs. Electric Field (all parameters other than electric field are standard, see Table III).

[20] Energy Spread and Virtual Source Size vs. Path Length (all parameters other than path length are standard, see Table III).

[21] Energy Spread and Virtual Source Size vs. Beam Half Angle (all parameters other than angle are standard, see Table III).

[22] Energy Spread and Virtual Source Size vs. Initial Kinetic Energy (all parameters other than initial energy are standard, see Table III).

[23] Energy Spread and Virtual Source Size vs. Initial Energy Spread (all parameters other than initial energy spread are standard, see Table III).

[24] Experimental evidence for the $IM^{1/2}$ dependence on the energy spread.

[25] Time distribution of particles in the initial and final planes with all parameters at standard values (see Table III) compared with a Poisson distribution.

[26] Same as above but a current of $10\mu A$ was used.

[27] Trajectory Slope vs. Radial Displacement in the virtual source plane with all parameters at standard values (see Table III).

[28] Current Density vs. Radial Displacement in the virtual source plane with all parameters at standard values (see Table III).

[29] Angular Intensity vs. Beam Angle in the reference plane at 1, 5 and 10μA with all other parameters at standard values (see Table III).

[30] Angular Intensity vs. Beam Angle in the reference plane at 1 and 100 amu with all other parameters at standard values (see Table III).